Politecnico di Torino

MASTER'S DEGREE IN BIOMEDICAL ENGINEERING

COMPARING THE PERFORMANCES OF DIFFERENT DIVERGENCE-FREE APPROACHES TO INCREASE THE ACCURACY OF 4D FLOW MRI VELOCITY DATA

Master's thesis by

ANTONELLA PIRRELLO

Supervisor:

Prof. UMBERTO MORBIDUCCI

Co-supervisors:

Dr. VALENTINA MAZZI

Dr. KAROL CALO'

A.A. 2023/ 2024

SUMMARY

Abstract

Cardiovascular diseases (CVDs) are the leading cause of global death, accounting for 30% of all fatalities. The understanding of the hemodynamics of cardiovascular flows in vivo is important to evaluate diseases progression and the efficacy of surgical treatments.

A new promising diagnostic technique for cardiovascular flow assessment is "4D flow MRI". It overcomes the limitations associated with traditional methods, like Doppler echocardiography and 2D time-resolved phase-contrast (PC) MRI and it is able to provide information on the temporal and spatial evolution of 3D blood flow, with complete volumetric coverage.

However, noise-like errors significantly affect the accuracy of these measurements. In this context, the aim of this study is to enhance the quality of 4D flow MRI data by exploiting the physical law of the incompressibility of blood, which results in the imposition of a divergence-free condition on the flow field.

In particular, three divergence-free approaches - Finite Difference Method (FDM), Divergence-Free Wavelets (DFW) and Radial Basis Functions (RBF) based methods – have been considered in this study to reduce the divergence of the velocity field provided by 4D flow MRI, reducing the deviation between the filtered flow field and the measured one.

In detail, the Finite Difference Method (FDM) projects the velocity data into a divergence-free space using Helmholtz-Hodge decomposition, solved by employing first-order finite differences with periodic boundary conditions.

Radial Basis Functions (RBF)-based method used normalized convolution to locally approximate the acquired velocity field into divergence-free radial basis functions (RBFs), used as convolution kernels. The normalized convolution operation is equivalent to solving a weighted linear least squares problem, the result of which is a vector of coefficients that is used to reconstruct the divergence-free flow field.

Divergence-Free Wavelets (DFW)-based method applies the Discrete Wavelet Transform, realized through a bank of filters, separately, to each velocity component. The resulting divergence-free and non–divergence-free coefficients, linearly combined, provide a sparse representation of flow data, which were subjected to the denoising procedure using a soft-thresholding technique, called SureShrink. Furthermore, a second-generation denoising method, named "cycle spinning", was considered to reduce blocking artifacts.

Comparative analysis of these methods, applied on synthetic velocity data obtained from a CFD simulation of a realistic aorta at the systolic peak and with Gaussian noise superimposed, demonstrated, both qualitatively and quantitatively, the effective restoration of the original flow field and a reduction in the divergence of noisy data.

Quantitative results showed that the DFW-based method performed better than FDM and RBF-based method. The no-divergence constraint in the DFW-based method is more relaxed,

making it less sensitive to segmentation errors Moreover, the DFW-based method with partial cycle spinning further enhanced its performance.

In conclusion, the finding of this study can be significant because the integration of these denoising techniques into 4D flow MRI data could improve the accuracy of hemodynamic assessments, providing a significant advance in the diagnostic and therapeutic management of cardiovascular disease.

INTRODUCTION

Cardiovascular diseases (CVD) are the most common cause of death worldwide (30% of all global deaths) (Gasteigder et.al. , 2014). Relevant examples of CVDs are acquired or congenital heart failures, stenosis, aneurysms (A. Can, R. Du., 2015) and atherosclerosis. The initiation, progression and outcome of a CVD is a multi-factorial problem that involves three different risk factors: systemic factors, related to diet and lifestyle, biological factors like wall biomechanics, genetics and vessel morphology and hemodynamic factors, related to the presence of disturbed flows within the vessels.

Cardiovascular pathologies arise in regions of complex geometry, characterized by multidirectional fluid dynamic patterns, like for example flow separation and recirculation.
The knowledge of cardiovascular flows allows to understand how altered hemodynamics contribute to the onset or progression of diseases (A.M. Nixon, M. Gunel, B.E. Sumpio.) and to evaluate the recovery of physiological flows following surgery or a surgical procedure.

The lack of a "gold standard" as a measurement technique for cardiovascular flow assessment in vivo and non-invasively, has involved different research to overcome the limitations of the most common clinical tools used for this purpose nowadays. They are:

- Doppler echocardiography: it measures a single direction of blood flow velocity through the emission of high frequency sound waves (2 to 18 MHz), by exploiting the Doppler effect for interpreting the receiving echoes.
  This approach is limited by the constraints associated with echo-Doppler imaging: variable velocity assessment, limited acoustic window and operator-dependent quality.
- 2D time-resolved (CINE) phase-contrast (PC) MRI: it involves velocity encoding in a single direction, perpendicular to the 2D imaging slice positioned orthogonally to the lumen of the vessel (through-plane encoding). As a result of incomplete spatial volume coverage, caused by gaps between adjacent slices, and breath-hold misregistration, caused by data acquisition performed during a 10-20 second breath-hold period, it is difficult to fully analyse flow patterns.

However, in the last decade comparative studies among the main techniques used in clinical practice for characterizing hemodynamic patterns in the human body (Maya Gabbour, Susanne Schnell, Kelly Jarvis, Joshua D Robinson, Michael Markl, Cynthia K Rigsby., 2014), have highlighted the potential of a new imaging tool, the 3D time-resolved PC-MRI, also known as 4D flow MRI. Even if 4D flow MRI performs worse in spatial and temporal resolution, compared with echo-Doppler, it overcomes 2D CINE PC MRI and Doppler echocardiography since it allows three-directional measurements of blood flow, flexible retrospective quantification of flow parameters, full volumetric coverage and hence more appropriate quantitative velocity measurements. However, noise-like errors significantly affect the accuracy of velocity measurements so the development of new clinical tools for assessing cardiovascular flows in vivo has increased the need to find techniques to increase their accuracy.

The aim of this study is to compare the performances of different state-of-the-art techniques to enhance the quality of 4D flow MRI velocity data by exploiting the physical law of the incompressibility of blood, which results in the imposition of a divergence-free condition on the flow field, by using synthetic 4D flow MRI data derived from a CFD simulation of a realistic thoracic aorta to which Gaussian noise was superimposed after the voxelization process.

MAGNETIC RESONANCE IMAGING (MRI)

Magnetic Resonance Imaging (MRI) techniques are based on the principle of Nuclear Magnetic Resonance (NMR), a spectroscopic imaging technique that provides information about the chemical-physical nature of matter through interaction at the nuclear level with magnetic fields (Hornak, 1996). This phenomenon was first observed in 1946 by E. Purcell and F. Bloch, winners of the Nobel Prize in Physics in 1952. However, it was applied to clinical diagnostics since the beginning of the 1970s, in view of its ability of producing images of body districts noninvasively and without the use of ionizing radiation (Bistolfi, 1986).

NUCLEAR MAGNETIC RESONANCE - PHYSICAL PRINCIPLES

Hydrogen is the most widely used nuclide in MRI, since it is abundant in biological tissues.

Each hydrogen atomic nucleus possesses a proton, which has an intrinsic magnetic property called spin. Spin has the dimensions of the physical entity 'angular momentum' and is generated by the rotation of the particle around its axis.

The rotation of a charged particle, such as the proton, produces a microscopic vector, parallel to the spin axis and aligned with the angular momentum or spin momentum I, which is called the magnetic moment (μ). So, the behaviour of the proton can be likened to that of a small magnet with a north pole and a south pole. As such, it can change orientation when immersed in an external magnetic field.

For a proton, with spin number ½, only two orientations are possible for the magnetic moment vector, each of which determines an energy configuration: high-energy (termed spin-down) or low-energy (termed spin-up).
The external magnetic field also exerts a mechanical moment on the spin, which produces precession motion in the spin around the flux lines of B_0, with a frequency described by Larmor's law:

$$\Omega_0 = \gamma B_0 \qquad (1)$$

where Ω_0 is the Larmor pulsation, γ is the gyromagnetic ratio and B_0 the external magnetic field strength.

Under conditions of rest, the magnetic moments are randomly oriented, and all orientations are equiprobable. The application of the external static magnetic field introduces orientations that are preferential to others, so globally a nonzero magnetization vector arises along the direction of magnetic field application B_0 (z axis). The component on the (x, y) plane, on the other hand, since the spins precede at the same frequency but with random phase, is zero.
The information needed for MR imaging is contained in the magnetization vector. It, however, is a sum of parallel and antiparallel contributions with respect to one direction, with a very low predominance of one group over another.

If all nuclei immersed in the B_0 field are considered, it is observed that the spin-up number (N_{up}) is slightly higher than the spin-down number (N_{down}) and their ratio is defined by the Boltzmann statistic:

$$N_{up}/N_{down} = e^{\frac{\Delta E}{kT}} \quad (2)$$

Where ΔE is the energy difference between the two energetic states N_{up} and N_{down}, k is the Boltzmann constant, and T is the absolute Temperature. This results in a low value of the magnetization vector, which in turn leads to low signal-to-noise ratio (SNR), poor detectability and measurement problems. To solve this problem, the phenomenon of resonance, the particular condition of a system whereby it has an excitation response that is maximally amplified, is exploited.

To place the system in a resonant condition, an additional external field must be provided at an appropriate frequency.

The stimulation magnetic field B_1, a dynamic field generated by a radio-frequency excitation with a pulsation equal to the Larmor pulsation, perpendicular to B_0, causes a transfer of energy from the stimulation field to the spin.

Under the effect of the magnetic field B_1, the magnetization vector deviates from the z-axis by an angle called the flip-angle (α). The value of the flip-angle depends on the duration of application of the B_1 field. α values of interest are:

- α=90°: the system is in saturation, the longitudinal component of the magnetization vector is cancelled and a transverse component arises in the (x, y) plane.
- The saturation of the system is caused by the transition of spins from spin-up to spin-down due to energy transfer, until the condition $N_{up} = N_{down}$ is reached, resulting in a cancellation of longitudinal component of the magnetization vector (M_z). In addition, the action of B_1 puts the spins in phase concordance. As the precession of these spins continues around the z axis, there is the appearance of a component of the resulting magnetization vector in the (x, y) plane, M_{xy}.
- α=180°: the longitudinal component along z is flipped, and no component appears in the (x, y) plane.

When the flip angle reaches 90° or 180°, the B_1 perturbation stops, and the system returns to its equilibrium state through two relaxation mechanisms:

- Longitudinal relaxation, or spin-lattice: involves a gradual recovery of the longitudinal component of the magnetization vector.
- Transverse relaxation, or spin-spin: involves a gradual cancellation of the transverse component of the magnetization vector.

The two processes occur simultaneously, and both have an exponential trend, with different time constants: constant T_1 is the longitudinal (or spin-reticulum/lattice) relaxation time, while constant T_2 is the transverse (or spin-spin) relaxation time:

$$M_z = M_0 \left(1 - e^{-\frac{t}{T_1}}\right) \tag{3}$$

$$M_{xy} = M_{xy_0} e^{-\frac{t}{T_2}} \tag{4}$$

The change in the direction of the magnetization vector generates an induced electromagnetic field on a coil placed in the (x, y) plane. The signal received by the coil has a time course that tends to zero almost exponentially and is called FID (Free Induction Decay).

The FID signal, however, contains no information about the spatial location of the voxel that originated it. To trace the raw data back to an ordered map associated with the image, a technique based on the Fourier method is used: after demodulating the FID coming from a voxel (thus eliminating the fast oscillations due to the stimulation field) the frequency and phase information of each individual FID is combined (phase and frequency encoding, the latter obtained by applying field gradients along the axes). Thereby, pairs of values are obtained that uniquely identify the position in the plane of the voxel which generated that signal.

At the end of the process, by summing the contributions of all voxels, a space expressed in Fourier coefficients, called k-space, is obtained. That space, then, represents the coefficients of the 2D Fourier transform of the measured MR image; therefore, to trace back to the image, it is sufficient to apply the inverse Fourier transform to the k-space.

There are several modes of k-space acquisition, which are called trajectories. The most popular ones are Cartesian trajectory, Echo Planar Imaging (EPI), radial trajectory and spiral trajectory. The most widely used is the Cartesian mode, which acquires parallel and equispaced lines of k-space by proceeding sequentially. Its wide use is due to the good quality of the reconstructions, which do not suffer from artifacts as in the case of the other trajectories. The use of such a trajectory, however, implies very long acquisition times because of the need to repeat the RF stimulus for each line acquired.

PHASE-CONTRAST MRI (PC MRI)

Cardiovascular magnetic resonance imaging has undergone substantial developments over the last decades. Since its introduction in the late 1980s, PC MRI, also termed 'flow-sensitive MRI' or 'MR velocity mapping', has become a routine part of standard-of-care cardiac MRI (David T.Wymer, Kunal P. Patel, William F. Burke, Vinay K. Bhatia. , 2020). In most MRI examinations, phase data are not considered for image interpretation. However, in selected clinical cases such as evaluating blood flow in the heart and through vessels with 2D CINE PC MRI or 4D flow MRI, phase data provide useful information. These imaging modes are based on the phase data of all MRI signals, in order to obtain quantitative blood flow information. Signals deconstructed by Fourier analysis maintain their frequency and phase information.
The generation of a phase-contrast MRI image, for unidirectional velocity encoding, involves two acquisitions (Figure 1), each taken after the application of a linear bipolar gradient in the flow direction, with all parameters held constant but the linear bipolar gradient reversed in the second acquisition (Joachim Lotz, 2002).

Spins, which move in the direction of application of the first positive magnetic field gradient, G1, acquire a displacement in their rotational phase, proportional to the position they have along the gradient and, therefore, to the velocity: faster spins, that reach positions where the gradient field takes on higher values, will have larger phase shifts than slower spins. The phase shifts of stationary spins are removed by the application of the second negative magnetic field gradient, G2, which is applied in the direction of the flow, with the same amplitude but reversed in sign with respect to G1.

However, since removal of the stationary signal is a source of noise in most phase-contrast images, a second acquisition with inverted bipolar gradient is performed and subtracted from the first one. This removes background phase effects and produces a map where only voxels in which the spins are moving will have a nonzero phase shift value, that is directly proportional to the blood velocity value.

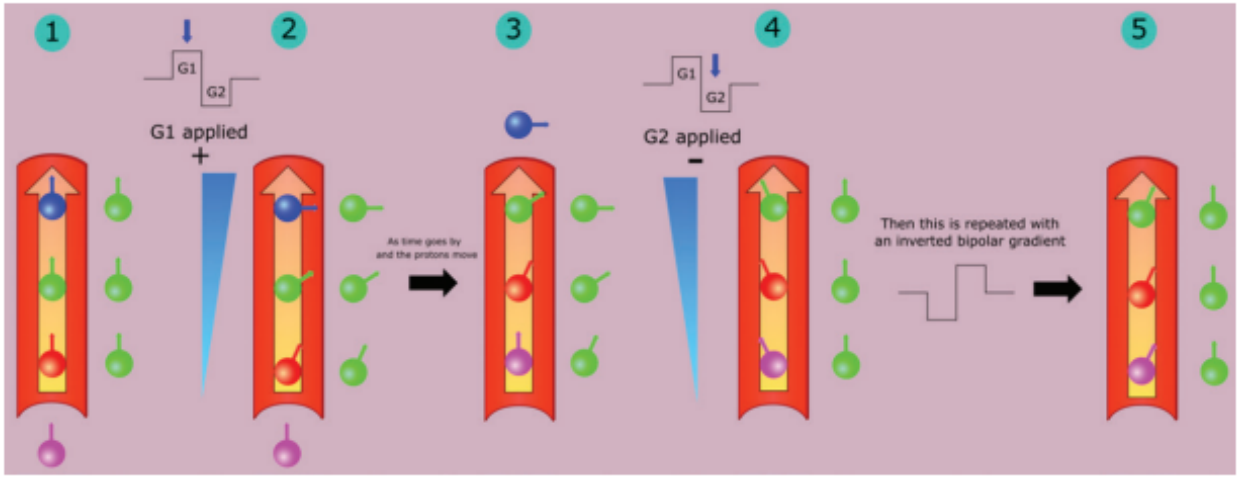

Figure 1. Physics of PC MRI processing: application of bipolar gradients.

The equation for calculating the spin phase change is:

$$\Delta\Phi = \gamma \vec{v} \Delta M_1 \tag{5}$$

where γ is the gyromagnetic ratio, $\vec{v}$ is the proton velocity and ΔM_1 is the change in the magnetic moment. The phase angle is directly proportional to the proton velocity. However, since the angles are finite and behave according to modular arithmetic, only a certain range of velocities can be mapped, those generating phase shifts that do not exceed the range that includes values from - 180° to 180°. The maximum measurable velocity is called the encoding velocity (Venc).

Since $\Delta\Phi < \pi$, when $\Delta\Phi = \pi$ $|\vec{v}| \leq$ Venc:

$$Venc = \frac{\pi}{\gamma \Delta M_1} \tag{6}$$

where ΔM_1 is proportionate to gradient strength. Since velocity encoding is inversely proportional to gradient intensity, encoding lower velocity requires larger gradient areas and thus longer echo and repetition times (TE and TR). Echo Time (TE) is the time between the application of the radio frequency (RF) stimulation and the moment when the echo signal is acquired. Repetition Time (TR) is the time interval between two successive excitation RF impulses applied to the same volume of blood.

Encoding velocity is defined as the maximum velocity that can be detected correctly without incurring the phenomenon of velocity aliasing. The latter generates an artifact in the image, identifiable as a sudden change from high to low velocity within a flow region. If aliasing artifacts are present, accurate visualization and quantification of the flow may be compromised, unless an antialiasing correction is made, or the acquisition is repeated by setting a higher Venc.

However, Venc is related to the SNR (or VNR in this case) by the following relationship:

$$Vnoise \approx \frac{Venc}{SNR} \tag{7}$$

Where V_{noise} represents the threshold below which speed measurement can be considered unreliable due to noise. So, a too high Venc can lead to increased noise superimposed on the image, resulting in a loss of image quality. Venc should be set at the physiological velocity of the vessel of interest and adapted to the hemodynamic conditions there. Typical settings for Venc are 150-200 cm/s in the thoracic aorta, 250-400 cm/s in the aorta with aortic stenosis or coarctation, 100-150 cm/s for intracardiac flow, and 50-80 cm/s in the large vessels of the venous system. If a large imaging volume with several vessels is examined, there may not be an optimal Venc setting, and the value must be chosen according to the clinical question.

4D FLOW MRI – INTRODUCTION

4D flow MRI technique uses the physical principles underlying PC MRI. It has been developed to overcome the limitations of 2D CINE PC MRI and perform more complete and better assessments on blood flow through the heart and large vessels.

4D flow MRI can provide information on the temporal and spatial evolution of 3D blood flow with complete volumetric coverage of any cardiac or vascular region of interest in a single acquisition, therefore it has become a new potential clinical diagnostic tool (Michael Markl, 2012) (Zoran Stankovic, Bradley D. Allen, Julio Garcia, Kelly B. Jarvis, Michael Markl. , 2014).

4D flow MRI is also known as three-dimensional (3D) time-resolved (CINE) phase-contrast (PC) MRI with three-directional velocity encoding. The method mentioned above obtains, for each voxel of an acquired 3D volume, at each measured time point of the cardiac cycle, anatomical and three-directional velocity information.

4D FLOW MRI – ACQUISITION TECHNIQUES

4D flow MRI, through four-point interleaved velocity encoding and the k-space segmentation technique, provides three-directional velocity measurements. Data acquisition is synchronized with the cardiac cycle and flow data are collected over multiple RR intervals of succeeding cardiac cycles.

According to the k-space segmentation technique, for each single line of raw k-space data, one reference image and three other images, each related to velocity encoding along three orthogonal x, y and z directions, are acquired.

Concomitantly, the k-space segmentation technique involves collecting, for each time frame of a cardiac cycle, a subset, N_{Seg} ,of all the steps required for phase encoding: a certain number of k-space lines along the y (N_y) and z (N_z) directions. The acquisition is repeated for each same time frame of successive cardiac cycles, until the entire three-dimensional coverage is achieved, after $\frac{N_y N_z}{N_{Seg}}$ heartbeats. The choice of N_{Seg} determines the temporal resolution, that is the time required to collect data in a single time frame, and consequently the total scan time.

At the end of the 4D flow data acquisition (Figure 2), four time-resolved 3D data sets are generated ("magnitude" data representing anatomy and three “phase” data sets representing "Vx, Vy and Vz" velocities). The large amount of data that must be collected results in significant scan times, and this is the primary cause limiting the use of 4D flow MRI in clinical practice.

Approaches that have been proposed to reduce scan times include the use of undersampling methods, like kt-BLAST, kt-SENSE, ktGRAPPA, L1-SPIRiT or other parallel imaging or compressed sensing techniques.

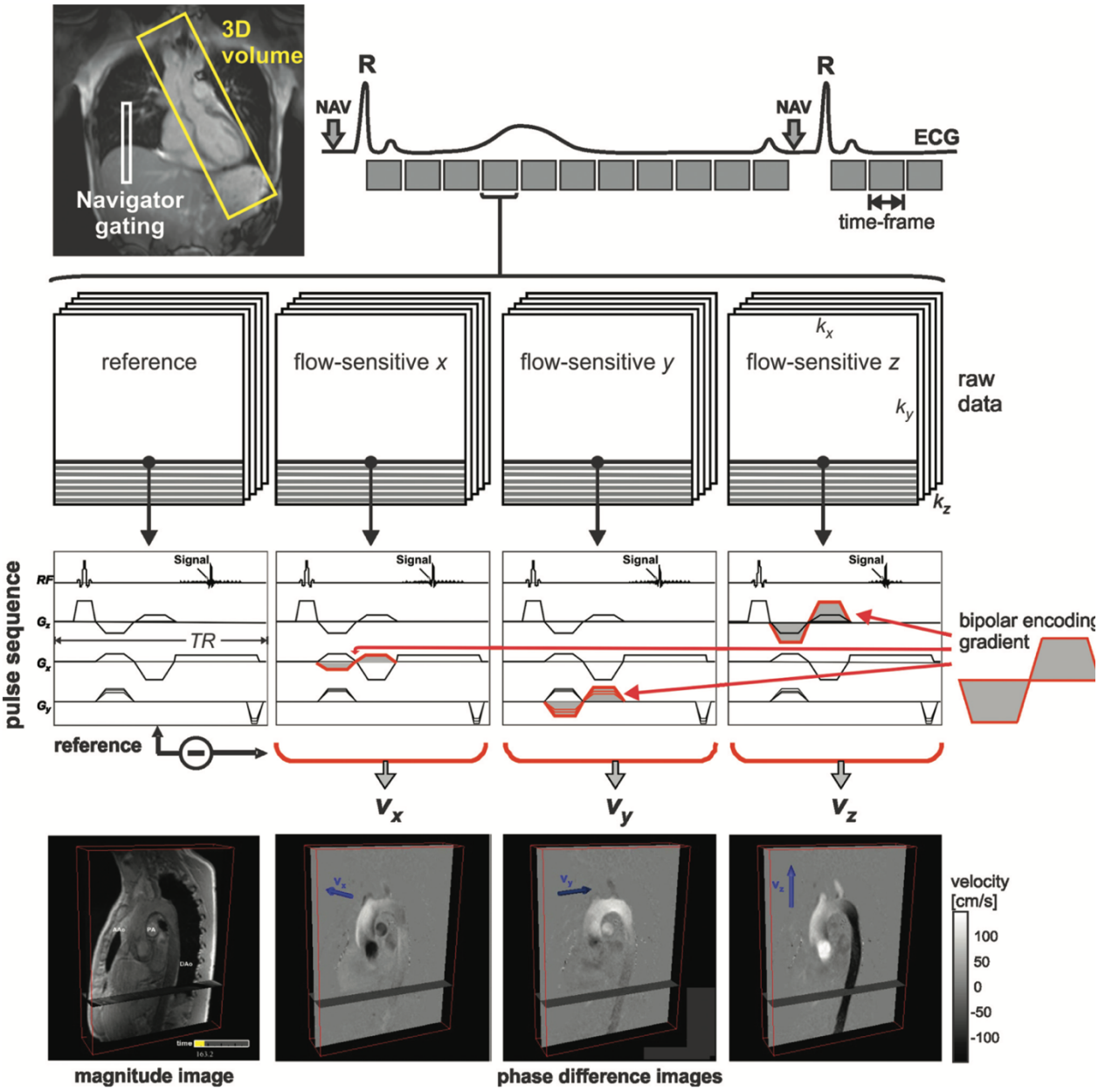

Figure 2. Standard data acquisition for 4D flow MRI.

4D FLOW MRI – LIMITATIONS OF THE TECHNIQUE

Current limitations of 4D flow MRI are: low spatio-temporal resolution, long scan times and acquisition noise (Malenka M. Bissell, 2023). The large volume of data collected in 4D flow MRI limits the spatio-temporal resolution (1.5-3 mm is the isotropic spatial resolution and 30-60 ms is the typical temporal resolution, in clinical settings). Furthermore, if undersampling techniques are not used, scan times can exceed 20 minutes. The acquisition noise causes multiple sources of error (Table 1) in 4D flow MRI, which degrade image quality and measurement accuracy, by introducing inaccurate flow quantifications. There are two main broad categories of errors that are reported below.

- Data acquisition-related errors

Data acquisition-related errors are background phase offsets due to magnetic field inhomogeneities, eddy currents, or even concomitant gradient fields. Background phase offset errors caused by concomitant gradient fields can be corrected by a scheme already implemented in most modern MRI systems, during the image reconstruction phase. Instead, those caused by eddy currents need a pre-processing phase to be corrected. Specifically, the switching of time-varying magnetic field gradients causes changes in magnetic flux that, in turn, induce eddy currents in the conductive parts of the scanning system. These eddy currents alter the strengths and durations of the desired gradients and thus result in spatially and temporally variable phase offsets in any type of PC-CMR. The recommended approach for correcting such offset errors is that presented by Walker et al. (Walker PG, 1993). The latter is based on the identification, following a thresh-holding procedure, of regions of static flow that are fictitious by polynomial interpolation on the image, to identify and subsequently subtract from the image the phase offsets caused by eddy currents. More details on appropriate correction strategies for background phase offsets due to magnetic field inhomogeneities can be found in Markl et al. (Markl M, 2003).

Other sources of error related to data acquisition include low spatial and/or temporal resolution and inadequate Venc, which, as discussed earlier, can cause phase unwrapping, resulting in velocity aliasing.

- Patient-related errors

Patient-related errors are caused by heart-rate variability, physiological respiration and unwanted body motion by uncooperative patients. Mainly due to respiratory movements, in clinical thoracic and abdominal applications, some artifacts are formed, resulting in reduced image quality that can be improved by respiratory gating, auto gating or even averaging techniques, which, however, result in increased scan time.

Source of error	Type of error	Consequences	Mitigation strategy
Acquisition related	Background phase offset	Inaccurate velocities and flow	Use stationary flow fit
	Low spatial and/or temporal resolution	Underestimation of peak flow and other quantitative parameters	Adapt to the region of interest, with at least 5–6 voxels across the vessel diameter
	Inadequate Venc	Aliasing or low SNR or VNR	Set Venc to 90% of expected velocity and use unaliasing post-processing
	Inadequate FOV	Too big: acquisition time too long, resolution too low Too small: region of interest not covered, spatial aliasing	Cover region of interest
	Acceleration parameters too high	Low SNR, blurring, spatial artifacts, underestimation of velocities	Adapt parameter to sampling technique, magnetic field, coils, contrast
	Intravoxel dephasing due to turbulence	Underestimation of velocities	Increase spatial resolution, reduce echo time
Patient related	Heart rate variability	Blur	Use arrhythmia rejection algorithm, prospective gating
	Respiratory motion	Respiration artifacts (ghosting, streaks, blurring)	Use respiratory gating, soft gating, averaging
	Other motion	Blur	Work with the patient; use a shorter scan time
	Overweight	Low SNR	Use contrast
Processing related	Inadequate volumetric segmentation	Loss of measurement accuracy	Complete a visual check; provide training
	2D retrospective slice placement non-orthogonal to flow	Underestimation of velocities and flow	Use automated placement or a dedicated tool; provide training
	Inter- and intraobserver variability	Reproducibility	Use automated segmentation; provide training to observer

Table 1. Typology, implication and proposed mitigation strategies for potential sources of errors in 4D flow MRI.

Despite the implementation of various techniques for reducing error sources, nonuniformly distributed noise and residual aliasing may still be present on the image, especially if the image has been reconstructed using subsampling methods to reduce scan times.

As will be explained in the next paragraphs, one approach to reduce residual errors is to constrain the data according to the physical law governing blood flow: the physical constraint of incompressible blood flow results in the imposition of a divergence-free condition on the velocity flow field acquired with 4D flow MRI.

ANATOMY AND PHYSIOLOGY OF THE AORTA

The divergence-free denoising techniques were tested on CFD simulation of incompressible blood flow within an aorta at the systolic peak. The aorta is the main artery of the human body, both in terms of size and elasticity (Cira Rosaria Tiziana di Gioia, 2023) (Xiaochen Wang, 2023). It is approximately 30-40 cm in length: it originates from the ejection cone of the left ventricle and first travels upward, after which it curves and finally returns downward, descending along the spine to pass the diaphragm and end at the level of the joint between the lumbar L4 and L5 vertebrae, bifurcating into the two iliac arteries. At its exit from the heart, its diameter measures about 3 cm and decreases in a craniocaudal direction.

The role of the aorta is to distribute oxygen-rich blood through the systemic circulation to lower caliber arterial vessels; these, in turn, repeatedly branch off to vascularize tissues throughout the body. Constant blood flow in the secondary arteries is also ensured thanks to the marked elasticity of the walls of the aorta.

The aortic wall (Figure 3) is made up of three overlapping tunics named the intima, media and adventitia, respectively, from the internal to the external surface of the aorta (D'amati, et al., 2013).

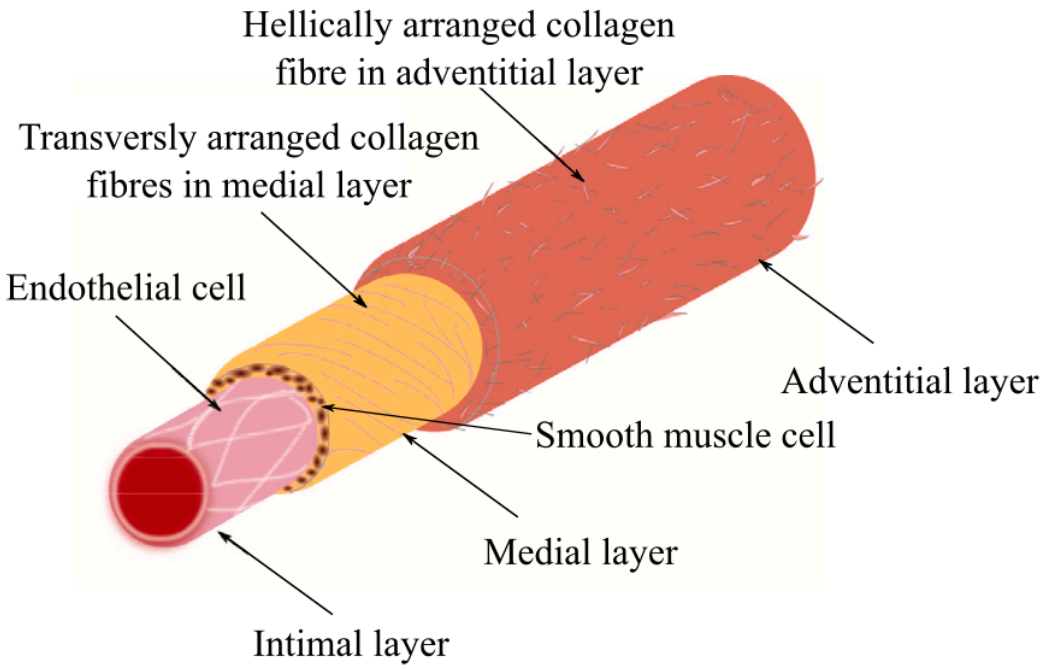

Figure 3. Composition of the aortic wall.

The tunica intima consists of endothelial cells, arranged on a thin connective layer called the basal lamina. The layer of endothelium comes in direct contact with blood, contains collagen and elastin fibers, so it is sensitive to pulsatile shear stress exerted by the streaming blood.

The middle tunica consists mainly of collagen, elastin, and smooth muscle cells (MSCs): it is the thickest layer of the artery wall, i.e., the one that supports loads under physiological conditions.

The adventitia tunica consists of connective tissue, supports loads at higher pressures, preventing the aorta from over-expanding, and collects the vasa vasorum, i.e., the vessels that sustain the arterial wall itself.

The thickness of each layer varies and depends on the distance from the heart.

The aorta is typically divided into two anatomical segments: the thoracic aorta and the abdominal aorta, separated by the diaphragm (Figure 4). The thoracic aorta is the portion above the diaphragm, which in turn is divided into the ascending aorta, aortic arch and descending aorta.

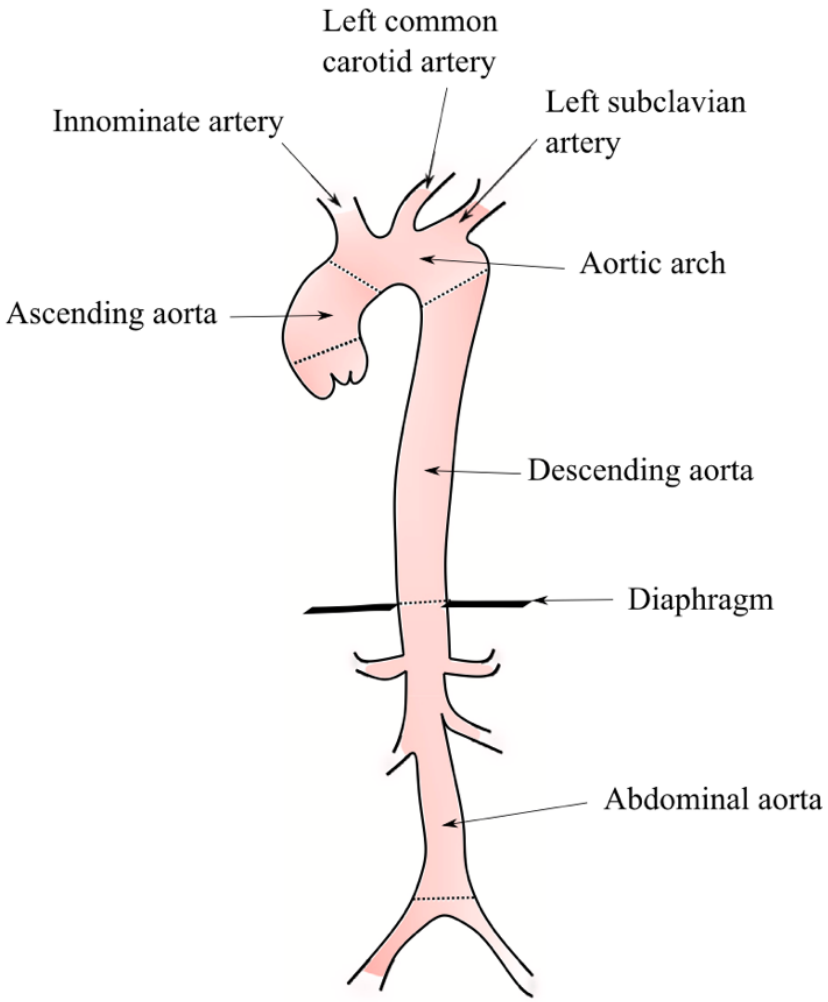

Figure 4. Aorta's anatomical segments.

ASCENDING AORTA

The ascending aorta is the first short segment of the aorta. It originates from the orifice of the aortic valve at the level of the third intercostal space, after which it heads upward and to the right until it reaches the second chondro-sternal articulation, where it terminates before the aortic arch. Approximately five centimeters long, the ascending aorta can be divided into two tracts: the aortic root, which extends from the annulus to the sinotubular junction (STJ) and includes the sinuses of Valsalva, three swellings posterior to each of the three valve leaflets, the aortic cusps end the origins of the coronary arteries and a very simple tubular tract that extends to the aortic arch.

AORTIC ARCH

The aortic arch originates where the ascending aorta ends, i.e., at the level of the second chondro-sternal articulation, carries upward and posteriorly and peaks at the level of the first chondro-sternal articulation, then descends posteriorly to the left and rests on the spine, to end at the level of the articulation between T4 and T5, where it terminates before the descending aorta. Three large arterial trunks perfusing the upper half of the body originate from the aortic arch from right to left, which are: the right brachiocephalic artery, the left carotid artery, and the left subclavian artery.

DESCENDING AORTA

The descending aorta follows the aortic arch. It begins at the lower margin of the IV thoracic vertebra, descends into the thorax, following the midline of the spine and then enters the aortic orifice of the diaphragm, at the level of the XII thoracic vertebra and continues as the abdominal aorta.

The abdominal aorta begins at the diaphragmatic hole for the passage of the aorta and ends, having reached the fourth lumbar vertebra, by bifurcating into the two common right and left iliac arteries.

BLOOD – PHYSICAL PROPERTIES

Blood is a specialized body fluid whose main functions are:

- Transport of oxygen and nutrients to cells and tissues.
- Removal of waste materials and their subsequent transport to the kidneys and liver, which clean the blood.
- Transport of cells and antibodies to protect the body from diseases and infections.
- Regulation of body temperature.
- Formation of blood clots to prevent excess blood loss.

Blood (Tamas Alexy, Jon Detterich, Philippe Connes, Kalman Toth, Elie Nader, 2022) is a corpuscular fluid material, composed mainly of erythrocytes (RBC), biconcave disks about 8μm in diameter and 1-2μm in thickness, platelets and white blood cells, in small percentages. These corpuscular components are immersed in an aqueous medium containing protein and electrolytes (the plasma).

Plasma, the suspending medium for the cellular components of blood, plays an important function in moderating the physical properties of blood. The viscosity of plasma is determined principally by its protein content: fibrinogen is an important determinant of plasma viscosity, due to its high molecular weight (~340 kDa) and fibrous structure. Albumin also significantly impacts plasma and whole blood viscosity. Plasma is a Newtonian fluid whereby its viscosity is independent of the shear rate it is exposed to. Its normal value at 37°C is around 1.3 mPa s.

Precisely because of this multiphase nature, whole blood, i.e., the mixture of plasma and solid particles, configures as a non-Newtonian fluid, defined as a fluid with a shear rate dependent viscosity. Blood viscosity is derived from its shear rate- shear stress relationship. Viscosity depends on several factors intrinsic to the fluid, such as temperature, pressure, density, and composition (Table 2). Haematocrit, defined as the volume of RBC compared to total blood volume (normal range: 35–45%), is the primary determinant of blood viscosity.

The viscosity of whole blood demonstrates a non-linear decrease with increasing shear rate. The tendency for RBC to cluster is the primary determinant of blood viscosity at low shear, and the dispersion of these clusters aids in dramatically decreasing blood viscosity with increasing shear.

“Aggregating” factors of RBC are: high percentage of haematocrit, because higher RBC concentrations promote cell-cell contact, high concentration of plasma protein and particularly fibrinogen, elimination of negatively charged glycoproteins from the surface (e.g., sialic acid), increase of membrane fluidity of RBC. Instead, shear rate is considered a “disaggregating” factor given that rouleaux are only stable under a tolerable low shear rate.
From a hydrodynamical point of view, blood, being composed of a high percentage of water, behaves as an incompressible fluid: its density is constant and, in accordance with the principle of conservation of mass, the blood flow field is ideally solenoidal, i.e. divergence-free.

Component and % of blood	Subcomponent and % of component	Type and % (where appropriate)	Site of production	Major function(s)
Plasma 46–63 percent	Water 92 percent	Fluid	Absorbed by intestinal tract or produced by metabolism	Transport medium
	Plasma proteins 7 percent	Albumin 54–60 percent	Liver	Maintain osmotic concentration, transport lipid molecules
		Globulins 35–38 percent	Alpha globulins—liver	Transport, maintain osmotic concentration
			Beta globulins—liver	Transport, maintain osmotic concentration
			Gamma globulins (immunoglobulins)—plasma cells	Immune responses
		Fibrinogen 4–7 percent	Liver	Blood clotting in hemostasis
	Regulatory proteins <1 percent	Hormones and enzymes	Various sources	Regulate various body functions
	Other solutes 1 percent	Nutrients, gases, and wastes	Absorbed by intestinal tract, exchanged in respiratory system, or produced by cells	Numerous and varied
Formed elements 37–54 percent	Erythrocytes 99 percent	Erythrocytes	Red bone marrow	Transport gases, primarily oxygen and some carbon dioxide
	Leukocytes <1 percent Platelets <1 percent	Granular leukocytes: neutrophils eosinophils basophils	Red bone marrow	Nonspecific immunity
		Agranular leukocytes: lymphocytes monocytes	Lymphocytes: bone marrow and lymphatic tissue	Lymphocytes: specific immunity
			Monocytes: red bone marrow	Monocytes: nonspecific immunity
	Platelets <1 percent		Megakaryocytes: red bone marrow	Hemostasis

Table 2. Percentage of component, subcomponent, type of protein and electrolyte content (and their major function performed within the human body) of blood.

BLOOD - FLUID DYNAMIC BEHAVIOUR

The behaviour of a viscous fluid at the macroscopic level is described, in fluid dynamics, by the Navier-Stokes equations, a system of nonlinear partial differential equations (PDEs) (R. B. Bird, R. C. Armstrong, and O. Hassager., 1987).
It has not yet been possible to determine a closed-form solution to this differential problem. However, modern computational models, coupled with the remarkable capabilities of modern computers, have made it possible to determine approximate numerical solutions of the Navier-Stokes equations and some but a few analytical solutions under extremely simplifying assumptions made about the fluid under consideration.
The Navier-Stokes equations (Figure 5) are directly descended from the balance equations, applied to an open thermofluidodynamic system: the mass conservation equation, momentum conservation equation and total energy balance equation.

Coordinates: (x,y,z)
Velocity Components: (u,v,w)
Time : t Pressure: p
Density: ρ Stress: τ
Total Energy: Et
Heat Flux: q
Reynolds Number: Re
Prandtl Number: Pr

Continuity:

$$\frac{\partial \rho}{\partial t}+\frac{\partial(\rho u)}{\partial x}+\frac{\partial(\rho v)}{\partial y}+\frac{\partial(\rho w)}{\partial z}=0$$

X – Momentum:

$$\frac{\partial(\rho u)}{\partial t}+\frac{\partial(\rho u^2)}{\partial x}+\frac{\partial(\rho uv)}{\partial y}+\frac{\partial(\rho uw)}{\partial z}=-\frac{\partial p}{\partial x}+\frac{1}{Re_r}\left[\frac{\partial \tau_{xx}}{\partial x}+\frac{\partial \tau_{xy}}{\partial y}+\frac{\partial \tau_{xz}}{\partial z}\right]$$

Y – Momentum:

$$\frac{\partial(\rho v)}{\partial t}+\frac{\partial(\rho uv)}{\partial x}+\frac{\partial(\rho v^2)}{\partial y}+\frac{\partial(\rho vw)}{\partial z}=-\frac{\partial p}{\partial y}+\frac{1}{Re_r}\left[\frac{\partial \tau_{xy}}{\partial x}+\frac{\partial \tau_{yy}}{\partial y}+\frac{\partial \tau_{yz}}{\partial z}\right]$$

Z – Momentum

$$\frac{\partial(\rho w)}{\partial t}+\frac{\partial(\rho uw)}{\partial x}+\frac{\partial(\rho vw)}{\partial y}+\frac{\partial(\rho w^2)}{\partial z}=-\frac{\partial p}{\partial z}+\frac{1}{Re_r}\left[\frac{\partial \tau_{xz}}{\partial x}+\frac{\partial \tau_{yz}}{\partial y}+\frac{\partial \tau_{zz}}{\partial z}\right]$$

Energy:

$$\frac{\partial(E_T)}{\partial t}+\frac{\partial(uE_T)}{\partial x}+\frac{\partial(vE_T)}{\partial y}+\frac{\partial(wE_T)}{\partial z}=-\frac{\partial(up)}{\partial x}-\frac{\partial(vp)}{\partial y}-\frac{\partial(wp)}{\partial z}-\frac{1}{Re_r Pr_r}\left[\frac{\partial q_x}{\partial x}+\frac{\partial q_y}{\partial y}+\frac{\partial q_z}{\partial z}\right]$$
$$+\frac{1}{Re_r}\left[\frac{\partial}{\partial x}(u\tau_{xx}+v\tau_{xy}+w\tau_{xz})+\frac{\partial}{\partial y}(u\tau_{xy}+v\tau_{yy}+w\tau_{yz})+\frac{\partial}{\partial z}(u\tau_{xz}+v\tau_{yz}+w\tau_{zz})\right]$$

Figure 5. Navier-Stokes equations.

Regarding these equations, some aspects need to be clarified. To study the motion of a fluid there are two possible approaches: the Lagrangian and the Eulerian representation. The clear difference between the two lies in the fact that, while in the first-mentioned, one is supposed to follow the kinematic/dynamic evolution of a single elementary fluid particle, in the latter, the focus is on a fixed volume in space, called the control volume, going to study what happens to a given mass of fluid transiting there over time. Generally, in fluid mechanics, the Eulerian representation is used.

EULERIAN MASS BALANCE – DIVERGENCE FREE CONDITION

The Eulerian approach describes the motion of a fluid by expressing, at each point in the space occupied by the fluid, the density and velocity of the fluid itself as a function of time. Consider a parallelepiped-shaped element of infinitesimal volume $dV = dxdydz$. The mass contained at a given instant in the volume is ρdV, where $\rho = \rho(t, x, y, z)$ is a function, in general, of time and position. The derivative (rate of increase) in time of the mass of the infinitesimal volume is then defined by $\frac{\partial \rho}{\partial t} dxdydz$.

With reference to the following fixed volume element in space, one defines:

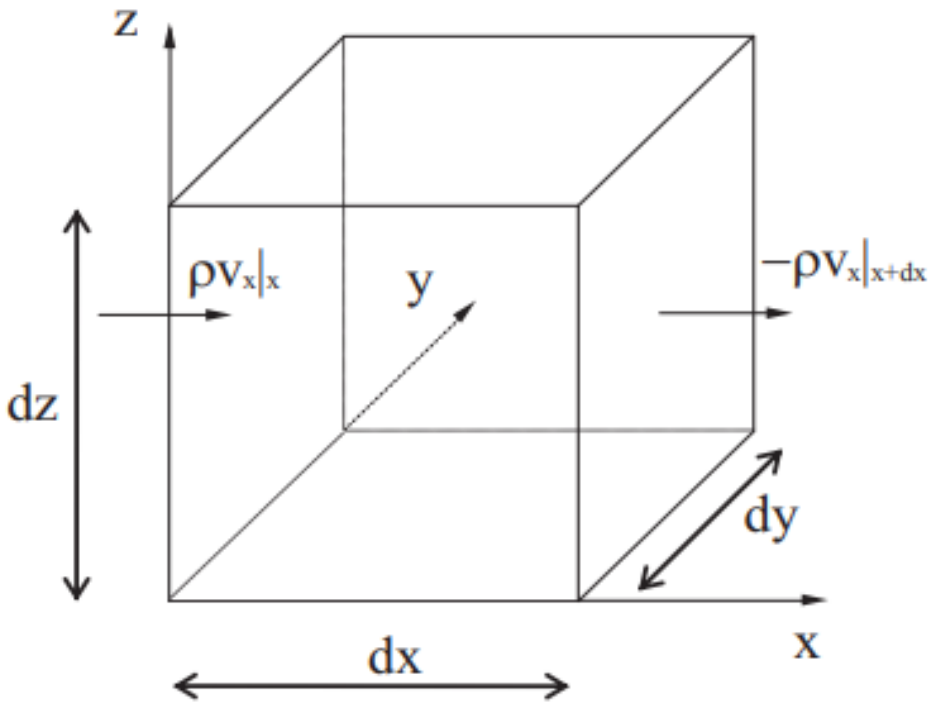

$\rho V_x|_x dydz$ incoming mass flow rate in dV across the surface in x

$\rho V_x|_{x+dx} dydz$ mass flow rate exiting dV through the surface in x+dx

$\rho V_y\big|_y dxdz$ incoming mass flow rate in dV across the surface in y

$\rho V_y\big|_{y+dy} dxdz$ mass flow rate exiting dV through the surface in y+dy

$\rho V_z|_z dxdy$ incoming mass flow rate in dV across the surface in z

$\rho V_z|_{z+dz} dxdy$ mass flow rate exiting dV through the surface in z+dz

Dealing with infinitesimals, under the assumption of continuum, one can go to the limits, to calculate the mass accumulated in the infinitesimal volume due to flow rates, first, in the x-direction. Assigning the positive sign to the incoming flow rate and the negative sign to the outgoing flow rate, the rate of increase of the mass within the infinitesimal volume, due to the flow through the surfaces in x and x+dx, divided by the volume of the cube, is:

$$\lim_{dx\to 0} \frac{\rho V_x|_x dydz - \rho V_x|_{x+dx} dydz}{dxdydz} = -\frac{\rho V_x|_{x+dx} - \rho V_x|_x}{dx} = -\frac{\partial \rho V_x}{\partial x} \tag{8}$$

The same can be done with respect to other coordinates:

$$\lim_{dy\to 0} \frac{\rho V_y\big|_y dxdz - \rho V_y\big|_{y+dy} dxdz}{dxdydz} = -\frac{\rho V_y\big|_{y+dy} - \rho V_y\big|_y}{dy} = -\frac{\partial \rho V_y}{\partial y} \tag{9}$$

$$\lim_{dz\to 0} \frac{\rho V_z|_z dxdy - \rho V_z|_{z+dz} dxdy}{dxdydz} = -\frac{\rho V_z|_{z+dz} - \rho V_z|_z}{dz} = -\frac{\partial \rho V_z}{\partial z} \tag{10}$$

he overall derivative (rate of increase) of the mass within the infinitesimal volume is due to the sum of the derivatives due to the flow through the surfaces in x and x+dx, y and y+dy, z and z+dz:

$$\frac{\partial \rho}{\partial t} = -\frac{\partial \rho V_x}{\partial x} - \frac{\partial \rho V_y}{\partial y} - \frac{\partial \rho V_z}{\partial z} \tag{11}$$

which can also be written as:

$$\frac{\partial \rho}{\partial t} + V_x \frac{\partial \rho}{\partial x} + V_y \frac{\partial \rho}{\partial y} + V_z \frac{\partial \rho}{\partial z} + \rho \frac{\partial V_x}{\partial x} + \rho \frac{\partial V_y}{\partial y} + \rho \frac{\partial V_z}{\partial z} = 0 \tag{12}$$

For incompressible fluid these relationships are simplified, since $\rho = \rho(t, x, y, z)$ is constant, and the equations just seen is reduced to:

$$\boldsymbol{\rho div V = 0} \tag{13}$$

DIVERGENCE OPERATOR

Divergence (Brewer, 1999) is an operator that converts a vector into a scalar quantity, given by the sum of the three partial derivatives of the three components of the vector along the x, y, z directions:

$$divV = \frac{\partial V_x}{\partial x} + \frac{\partial V_y}{\partial y} + \frac{\partial V_z}{\partial z} \tag{14}$$

In fluid dynamics, divergence can be interpreted as the overall difference between the flow entering and leaving the 6 faces of a cube of dimensions dx, dy, dz, within the fluid domain of interest.

Negative divergence indicates that the outflow is greater than the inflow and the flow tends to compress, that is, to converge to a point in the vector field.

If the divergence has positive values, the incoming flow is greater than the outgoing flow and the flow tends to expand, that is, to diverge from a point in the vector field.

A vector field in which the divergence representing it is zero is called a solenoidal field.

GRADIENT OPERATOR

The gradient operator (Weisstein) expresses the change in a scalar physical quantity per unit length in each direction. For example, the thermal gradient expresses the change in temperature along a chosen direction, while the pressure gradient, similarly, express the change in pressure along a particular direction. The gradient of a scalar function f(x,y,z) is defined as the vector, denoted by $grad\ f$, given by the sum of the three prime partial derivatives of the function along the three directions, identified through the three versors (representing the unit norm and direction vectors of the three Cartesian axes x, y and z) denoted by the letters i, j and k. In symbols:

$$grad\ f = \frac{\delta f}{\delta x} i + \frac{\delta f}{\delta y} j + \frac{\delta f}{\delta z} k \tag{15}$$

The gradient transforms a scalar into a vector.

DIVERGENCE-FREE STRATEGIES TO INCREASE THE ACCURACY OF 4D FLOW MRI VELOCITY DATA

By constraining the synthetic 4D flow MRI velocity data to the physical law governing blood flow, the Eulerian mass balance, under the assumption of incompressible fluid, the velocity field must ideally be divergence-free. Noise-like errors can be reduced by suppressing divergent components in the flow data. In this context, this study compares the performances of various divergence-free approaches exploiting the physical law of the incompressibility of blood to enhance the quality of 4D flow MRI velocity data.

These divergence-free strategies correct the divergence of the velocity field provided by 4D flow MRI, trying to keep it as close to zero as possible, while keeping the deviation between the denoised flow field and the measured flow field as small as possible.

Bakhshinejad et al. (Bakhshinejad., 2018), divided these techniques in two groups:

- *Projection-based methods,* where the divergence-free condition to the velocity is strongly imposed, through the projection of the unprocessed noisy 4D flow data into a divergence-free space.
- *Regularization-based methods,* where the divergence-free condition to the velocity is relaxed through mathematically rigorous spatiotemporal regularizations.

For this study, three state-of-the-art divergence-free projection-based methods have been considered:

- Finite Differences based Method (FDM).
- Radial Basis Functions (RBFs) based Method.
- Divergence-free Wavelets (DFWs) based Method.

FINITE DIFFERENCE METHOD

Finite difference methods are commonly used to solve differential equations by discretizing them, approximating the derivatives with the difference operation, by taking advantage of Taylor series expansion. Let f(x) be a continuous and n-times differentiable function. Its value at nearby points can be expressed in terms of a Taylor series:

$$f(x+\Delta x) = f(x) + \frac{df(x)}{dx}\Delta x + \frac{d^2f(x)}{dx^2}\frac{\Delta x^2}{2!} + \cdots + \frac{d^nf(x)}{dx^n}\frac{\Delta x^n}{n!} + \cdots \tag{16}$$

The series seen above converges if Δx is small, and f(x) is differentiable. For a convergent series, the successive terms are progressively smaller. The terms of the Taylor series expansion can be rearranged to give an accurate approximation of the first derivative:

$$\frac{df(x)}{dx} = \frac{[f(x+\Delta x) - f(x)]}{\Delta x} + o(\Delta x) \tag{17}$$

Both the spatial and temporal domains are discretized, i.e., divided into a finite number of intervals. The solutions at the grid points are obtained from the discretization operation, with a certain degree of approximation, the more exact the distance Δx, between the grid intersection points that overlap the domain of definition of the unknown function, decreases. The error between the numerical solution and the exact solution is determined by the error that is made by switching from the differential operator to the difference operator. This error is called discretization error or truncation error (of the Taylor series).

The finite difference method proposed by Song et al. (S. M. Song, 1993) computes the discretized form of the Helmholtz-Hodge decomposition (Harsh Bhatia, 2013) to project the 4D flow data into a divergence-free space.
The Helmholtz-Hodge decomposition (HHD) of a vector field is one of the fundamental theorems of vector calculus. In fluid dynamics, the use of the properties of HHD to smooth vector fields is particularly interesting.

According to Helmholtz, under conditions of asymptotic behaviour at infinity, every vector field in $\mathbb{R}^3$ can be described in terms of its divergence-free and rotation-free components:

1. The divergence-free component is incompressible, represents rotation, and can be expressed as the curl of a vector field.
2. The rotation-free component is irrotational, represents translation and compression/expansion, and can be expressed as the gradient of a scalar field.

Based on this theorem, every acquired vector field $\overrightarrow{v_M}$ can be expressed as follows:

$$\overrightarrow{v_M} = \nabla p + \nabla \times \vec{q} \tag{18}$$

Where ∇p is the irrotational (curl-free) contribution and $\nabla \times \vec{q}$ the incompressible (divergence-free) contribution. The calculation of the divergence of the velocity field $\overrightarrow{v_M}$ coincides with the calculation of the divergence of the gradient (Laplacian) of the scalar function p, since the contribution $\nabla \times \vec{q}$ is already divergence-free:

$$\nabla \cdot \overrightarrow{v_M} = \nabla^2 p \quad in\ \Omega \tag{19}$$

where Ω is the flow domain. One calculates p by solving the Poisson equation with boundary condition $p = 0\ in\ \partial\Omega$ using the Fast Fourier Transform with periodic extension and thus obtains the projection of $\overrightarrow{v_M}$ in the divergence-free space:

$$\mathbb{P}\overrightarrow{v_M} = \overrightarrow{v_M} - \nabla p \tag{20}$$

where $\mathbb{P}$ is the projection operator. Numerically $\mathbb{P}$ was implemented as:

$$\mathbb{P} = I - E^T(EE^T)^{-1}E \tag{21}$$

where E is the discretized divergence operator.

RADIAL BASIS FUNCTIONS – BASED METHOD

Busch et al. (J. Busch, 2013) used the normalized convolution to locally approximate the acquired velocity field into divergence-free radial basis functions (RBFs), functions of real variables with real values that depend exclusively on the distance from the origin or from a fixed point called the centre linearly combined to be divergence-free, used as convolution kernels.

NORMALIZED CONVOLUTION

Standard convolution is one of the most widely used operations in image processing, the process performing certain operations into a digital image, like denoising, to get some useful information from it. It is a simple mathematical operation in which two matrices (the image and a kernel) produce a third matrix as a result of the following processes:

- Superimposition of a kernel (or mask) on the image.
- Multiplication of coincident terms.
- Sum of the results and divide by the weight $\sum k_{ij}$.
- Moving the kernel to the next pixel (over the entire image matrix).

$$\frac{k_{11}I_{11} + k_{12}I_{12} + \ldots + k_{23}I_{23}}{|k_{11}| + |k_{12}| + \ldots + |k_{23}|}$$

I_{11}	I_{12}	I_{13}	I_{14}	I_{15}	I_{16}	I_{17}	I_{18}	I_{19}
I_{21}	I_{22}	I_{23}	I_{24}	I_{25}	I_{26}	I_{27}	I_{28}	I_{29}
I_{31}	I_{32}	I_{33}	I_{34}	I_{35}	I_{36}	I_{37}	I_{38}	I_{39}
I_{41}	I_{42}	I_{43}	I_{44}	I_{45}	I_{46}	I_{47}	I_{48}	I_{49}
I_{51}	I_{52}	I_{53}	I_{54}	I_{55}	I_{56}	I_{57}	I_{58}	I_{59}
I_{61}	I_{62}	I_{63}	I_{64}	I_{65}	I_{66}	I_{67}	I_{68}	I_{69}

K_{11}	K_{12}	K_{13}
K_{21}	K_{22}	K_{23}

The equation represents a weighted linear combination of values, used to estimate the output of an image processing operation such as image filtering. I_{ij} represents the intensity values of each pixel in the image. k_{ij} represents the weight coefficients associated with each intensity value I_{ij}. The numerator $\sum k_{ij}\, I_{ij}$ represents the weighted sum of pixel intensities. The denominator $\sum|k_{ij}|$ normalises the equation and is the sum of the absolute values of the weights.

Unlike standard convolution, in normalized convolution, both the data and the convolution operators are accompanied by a scalar component that represents the appropriate “weight” to be given to the data, the certainty function values, or to the operator values, the applicability function values. These special properties have largely enabled the use of normalized convolution in various applications, to reduce or eliminate false responses of the standard convolution operator due to missing or uncertain data: effects, called “edge effects”, that inevitably occur at the edges of limited input data. For a signal of limited extent, the surround of points near the boundary will include points where no values are provided.

Using a certainty function, the weight associated with such missing or unreliable data can be reduced by leaving the signal value unspecified and setting the certainty values at those points to zero or very low values.

In addition, the basis functions, in which the surroundings of a signal point are projected, can be defined for a domain larger than the surroundings under consideration: they can in fact be unlimited, e.g., polynomials or complex exponentials, and however take on a value of zero at points where one is not operating, thanks to the applicability function, which imposes a spatial localization or "windowing" of the convolution operator.
The appropriate choice of applicability function depends on the type of application. In general, there is a tendency to give greater importance to points in the centre of the surroundings under consideration than to points farther away. Therefore, unless specific direction dependence is desired, isotropic and monotonically decreasing applicability in all directions is preferred.

Normalized convolution is a point operation or, more correctly, an operation on a neighbourhood of each signal pixel, which can be better analysed when projected into a subspace which is spanned by a set of carefully chosen new basis functions. The projection is equivalent to solving a weighted linear least squares problem, whose weights are the values of the certainty function and of the applicability function. The geometric interpretation of least-squares minimization is that the local neighbourhood of the signal, for each pixel, is projected into a subspace spanned by the basis functions (Lowitzsch, 2002).

The result of normalized convolution at each point of the signal is a vector of coefficients. It is found using a weighted least square fit to the acquired 4D flow data, formulated as follows:

Let $t(r)$ be some arbitrary function in $\mathbb{R}$ and B a finite set of basis functions $b_1(r)$, $b_2(r)$, … $b_m(r)$ with $r \in \mathbb{R}^3$. We call:

$$t'(r) = \sum_{i=1}^{m} b_i(r)u_i \tag{22}$$

the best approximation of *t* in B if the coefficient u_i are chosen such that the supremum norm:

$$|t - t'| \equiv \sup_{r\in\mathbb{R}}\big(t'(r) - t(r)\big) \tag{23}$$

is minimal. According to the normalized convolution principle for the expansion into basis functions, the equation is modified as follows:

$$a(r)c(r)t'(r) = a(r)c(r)\sum_{i=1}^{m} b_i(r)u_i \tag{24}$$

Where a(r) and c(r) are the values, respectively, of the applicability function and the certainty function for each point of the image. Let the $n \times n$ $W_a = diag(a)$, $W_c = diag(c)$ two introduced matrices, containing the scalar values of a(r) and c(r), respectively, with the positions of the lattice points on the diagonal.
Referring to a discrete image, **t**, the equation can be rewritten as follows:

$$W_a W_c t' = W_a W_c B u \tag{25}$$

The coefficients of u are chosen such that $|t - t'|$ is minimal with respect to the Euclidean norm. A direct solution is obtained by:

$$u = (B^*(W_a W_c)^2 B)^{-1} B^*(W_a W_c)^2 t \tag{26}$$

which results in a system of equations given by:

$$u = \begin{pmatrix} (a \cdot c \cdot b_1, b_1) & \cdots & (a \cdot c \cdot b_1, b_m) \\ \vdots & \ddots & \vdots \\ (a \cdot c \cdot b_m, b_1) & \cdots & (a \cdot c \cdot b_m, b_m) \end{pmatrix}^{-1} \begin{pmatrix} (a \cdot c \cdot b_1, t) \\ \vdots \\ (a \cdot c \cdot b_m, t) \end{pmatrix} \tag{27}$$

The basis functions, in which the surrounding of a signal point is projected, must reflect the physical behaviour of the data: they must be divergence-free.
For this purpose, a class of matrix-valued radial basis functions, divergence-free and compactly supported, have been introduced.

Radial basis functions are functions of real variables with real values that depend exclusively on the distance from the origin or from a fixed point called the centre. More precisely, a radial basis function (RBF) is a function $\varphi: \mathcal{R}^n \to \mathcal{R}$ such that $\varphi(x) = \varphi(\|x - x_0\|)$, where $x = x_1, \ldots, x_n$ and $\|.\|$ is the Euclidean norm.

They are often used as a collection $\{\varphi_k\}_k$ which form a basis for some function space of interest, hence the name.

Commonly used type of RBF include:

- Gaussian

$$\varphi(r) = e^{-(\varepsilon r)^2} \tag{28}$$

- Inverse quadratic

$$\varphi(r) = \frac{1}{1 + (\varepsilon r)^2} \tag{29}$$

- Inverse multiquadric

$$\varphi(r) = \frac{1}{\sqrt{1 + (\varepsilon r)^2}} \tag{30}$$

Where ε is the shape factor.

- Polyharmonic spline

$$\begin{gathered} \varphi(r) = r^k \\ \varphi(r) = r^k \ln r \end{gathered} \tag{31}$$

- Thin plate spline

$$\varphi(r) = r^2 \ln r \tag{32}$$

Explicitly, the expansion of a function $f(x)$ in RBF will have the form:

$$f(x) = \sum_{i=1}^{N} a_i \varphi(\|x - x_i\|) \tag{33}$$

where the approximating function $f(x)$ is represented as a sum of N radial basis functions, each weighted by an appropriate coefficient a_i and associated with a different centre x_i, to be determined to minimize the error in a suitably chosen direction and thus optimize the approximating function.

Bush et al. (J. Busch et.al, 2013), introduced a set of RBFs defined based on the Gaussian function ψ

$$\psi_\gamma(r) = \exp\left(-\frac{|r|^2}{2\gamma^2}\right) \tag{34}$$

where γ determines the size of the support.

The divergence-free RBFs are given by:

$$\xi^i(r) = \sum_{j=1,2,3} \left(\frac{\partial^2}{\partial r_i \partial r_j} e_j - \frac{\partial^2}{\partial r_j \partial r_j} e_i\right) \Psi_\gamma(r) \tag{35}$$

where i count the the spatial dimension. It follows that the sum:

$$\sum_i (\xi^1(r - r_i)c_i^1 + \xi^2(r - r_i)c_i^2 + \xi^3(r - r_i)c_i^3 \tag{36}$$

is dense in the space of divergence-free functions where c_i^1, c_i^2, c_i^3 denote the coefficients for the expansion. This implies that, in theory, any divergence-free function can be approximated arbitrarily well by a linear combination of RBFs.

Using:

$$\Phi = (\xi^1 \xi^2 \xi^3) \tag{37}$$

the radial basis matrix can be written as:

$$\Phi(r) = \left[\left(1 - \frac{|r|^2}{2\gamma^2}\right) I + \frac{1}{2\gamma^2} r r^T\right] exp\left(-\frac{|r|^2}{2\gamma^2}\right) \tag{38}$$

where I is the identity matrix.
Finally, using matrix notation, the vector field is expanded into radial basis matrices according to:

$$v(r) = \sum_i \Phi(r - r_i)c_i \tag{39}$$

and the coefficients c_i^1, c_i^2, c_i^3 are summarized into a vector:

$$c_i = (c_i^1\ c_i^2 c_i^3)^T \tag{40}$$

The process of least square fit to the acquired 4D flow data, used to find the vector of coefficients, results in a system of equations given by:

$$\begin{bmatrix} \Phi(r_1 - n_1) & \dots & \Phi(r_1 - n_{n)} \\ \dots & \dots & \dots \\ \Phi(r_n - n_1) & \dots & \Phi(r_n - n_{n)} \end{bmatrix} \begin{bmatrix} c_1 \\ \dots \\ c_n \end{bmatrix} = \begin{bmatrix} V_1 \\ \dots \\ V_n \end{bmatrix} \tag{41}$$

here the locations r_i where the divergence-free velocity field is reconstructed are the same locations n where the 4D flow data is sampled.

The projection of the noisy data into divergence-free vector fields, using the finite difference method or even the radial basis functions (RBFs) used as convolution kernels in the normalized convolution operation, imposes a too rigorous divergence-free constraint on the 4D flow data, requiring accurate segmentation to avoid the possibility of significant divergent components arising in the neighbourhood of flow edges, static tissue or turbulent flow, where the discrete flow representation consists of discontinuities. Consequently, it was necessary to develop an algorithm that imposes a 'softer' no-divergence constraint on the flow data, reducing the sensitivity of noise reduction to segmentation errors, cause accurate segmentation is difficult to achieve when working with low signal-to-noise data, like those from 4D flow MRI.

DIVERGENCE-FREE WAVELETS – BASED METHOD

Ong et al. (F. Ong, 2015) proposed a robust process to enforce a soft divergence-free constraint on the flow field, using the divergence-free wavelet (DFW) transform.

WAVELET TRANSFORM

The wavelet transform is a powerful tool for the analysis and processing of signals and is extremely efficient in various fields of application, such as compression and denoising, and in general when dealing with non-stationary signals, such as images (A.Bovik, 2009).
These, in fact, are characterised by long period tendency at low frequencies (backgrounds), also called trends, and short period tendency at high frequencies (discontinuities, edges), also called anomalies. The latter, although they occupy a relatively small percentage in the image, have a high information content and must therefore be represented appropriately.

The wavelet transform has several interesting properties:

- Good time-frequency localization capability: it can analyze signals with time-varying characteristics (the images that needs to be analyzed has both slowly varying trends, like sine waves, and abrupt variations, like deltas).
- Multiresolution representation, through the separation of low-frequency and high-frequency contents by using two families of functions: scaling functions and wavelet functions.
- It is easily constructed through a filter bank.

The Wavelet transform is the best compromise in the trade-off between time resolution and frequency resolution in signal analysis.
To introduce the concept of time-frequency localization, reference should be made to the Fourier Transform and the Short Time Fourier Transform (STFT). The Fourier transform of an analogue signal x(t) is defined as follows:

$$FT[x(t)] = X(f) = \int_{-\infty}^{+\infty} x(t)e^{-j2\pi ft}dt \tag{42}$$

Where f is the frequency. The Fourier transform has perfect frequency localisation (Figure 6): it provides information about all the frequency components of the signal being analysed and their amplitudes but gives no information about when each frequency component of the signal appears over time. Thus, the Fourier transform is ideal for analysing stationary signals.

The STFT was developed to overcome the poor time resolution of the Fourier transform. It is mathematically defined as follows:

$$STFT[x(t)] = STFT[f,\tau] = \int_{-\infty}^{+\infty} x(t)g^*(t-\tau)e^{-j2\pi ft}dt \tag{43}$$

Here, f is the frequency, $g(t)$ is the convolution window of fixed length and τ is the time shift of $g(t)$ along the signal. STFT is the simplest way to obtain a time-frequency transform of the signal. The non-stationary signal is divided into several portions, assumed to be stationary, through convolution with a window $g(t)$ of fixed length. The window is translated from the beginning to the end of the signal and the Fourier transform is calculated for each stationary portion into which the signal has been divided.

Although the STFT has better temporal localization (Figure 7) than the FT, the use of a window of finite length results in a loss of frequency resolution compared to the FT.

A good time-frequency transform should have Δt (time resolution) and Δf (frequency resolution) very small; however, the uncertainty principle rules out the possibility of having an arbitrarily high resolution in both time and frequency, since it limits the duration-band product of the functions as follows:

$$\Delta t \Delta f = \frac{1}{4\pi} \tag{44}$$

This relationship is also called Heisenberg's inequality.

In two-dimensional signals, such as images, there are low-frequency components that last for a long time and require high frequency resolution and high-frequency components that appear as peaks in time and require high temporal resolution.

The wavelet transform (Figure 8), due to its property of providing multi-resolution analysis, has found numerous applications in the field of image analysis (I.Daubechies).

Multiresolution analysis provides:

- Good time resolution and poor frequency resolution at high frequencies.
- Good frequency resolution and poor time resolution at low frequencies.

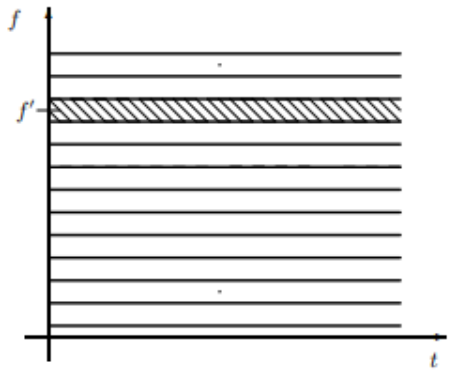

Figure 6. Time-frequency localization example for FT

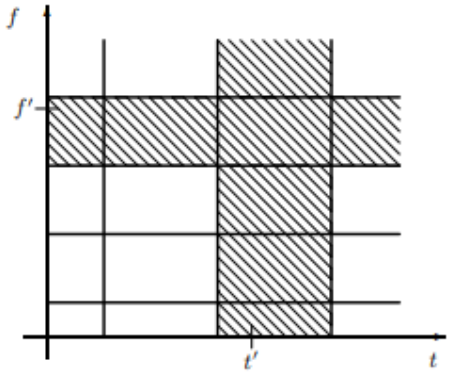

Figure 7. Time-frequency localization example for STFT

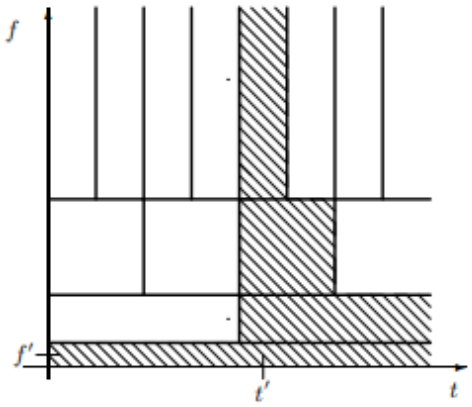

Figure 8. Time-frequency localization example for CWT

An important feature common to all wavelets is that they are bounded, i.e. they decline to zero in amplitude at some distance from the centre, in stark contrast to the sine/cosine waves used in Fourier analysis, which continue to infinity. This is the underlying key to DWT's temporal localisation. The two major transforms in wavelet analysis are continuous and discrete transform.

Mathematically, the Continuous Wavelet Transform (CWT) is defined as follows:

$$CWT[x(t)] = CWT[a,b] = \frac{1}{\sqrt{a}}\int_{-\infty}^{+\infty} x(t)\psi^*\left(\frac{t-b}{a}\right)dt \tag{45}$$

where $a = {}^{1}/_{frequency}$, is the scale parameter and $\psi^*\left(\frac{t-b}{a}\right)$ is obtained from the function $\psi(t)$, known as the mother wavelet.

The wavelet is a rapidly decaying wave like oscillation that has zero mean and finite energy. An example of a mother wavelet is shown in Figure 9, with the corresponding expanded (a > 1) and compressed version (a < 1).

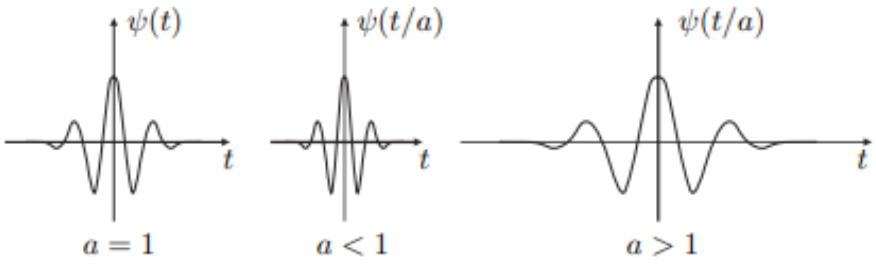

Figure 9. Mother wavelet (a=1) with corresponding expanded (a > 1) and compressed version (a < 1).

The wavelet constitutes a new basis function and acts as a window function, similarly to that of the STFT. Wavelet exists in different size and shape: to choose the right wavelet one will need to consider the application one will use for. Two important key wavelet concepts are scaling and shifting. By modifying a and b, the wavelet is respectively scaled (expanded and/or compressed) and shifted along the signal. Scaling refers to the process of stretching or shrinking the signal in time, which can be expressed using the equation $\psi\left(\frac{t}{a}\right)$, where $a > 0$ is the scaling factor. A larger scale factor a results in a stretched wavelet, which corresponds to a lower frequency. A smaller scale factor results in a shrinker wavelet, which corresponds to a higher frequency.

$CWT[a,b]$ represents how well the modified mother wavelet matches the signal. When wavelet and signal have similar frequencies, the local fit is good. Alternatively, when the frequency of the signal and the frequency of the wavelet are different, the wavelet does not align with the signal very well, so the local fit is bad. A stretched wavelet helps in capturing the slowly varying changes in a signal while a compressed wavelet helps in capturing the

abrupt changes. Shifting a wavelet means advancing the onset of the wavelet along the length of the signal.
The output of CWT are coefficients which are functions of scale (or frequency) and time. Several scales wavelets (typical number of scales per octave are 10,12,16 and 32) are shifted in time along the entire length of the signal and compared with the original signal. The process is repeated for all the scales resulting in coefficients that are function of wavelet scale and shift parameter. The time-frequency windows of $\psi_{ab}(t)$ have overlapped each other, which means there is information redundancy in CWT: if the scaling and shifting parameters are chosen to be discrete then the wavelet transform won't generate huge amounts of data and redundant coefficients are eliminated.

The Discrete Wavelet Transform (DWT) is mathematically defined as follows:

$$DWT[x(t)] = DWT[a,b] = \frac{1}{\sqrt{a}} \sum_{m=0}^{p-1} x[tm] \psi \left[\frac{tm - b}{a} \right] \tag{46}$$

with scaling and shifting parameters discretized as follows:

$$a = k2^{-j} \tag{47}$$

$$b = 2^{-j} \tag{48}$$

where j is the resolution level of the multiresolution analysis which will be discussed later and k is a discrete scaling parameter that regulates the level of wavelet expansion.
This process is often referred to as dyadic scaling and shifting because a and b change as a function of the power of 2. For the denoising and compression of signals and images the key application is the Discrete Wavelet Transform (DWT). To implement the DWT, one uses discrete filter banks (Figure 10) to compute discrete wavelet coefficients. Two-channel perfect reconstruction (PR) filter banks are a common and efficient way to implement the DWT.

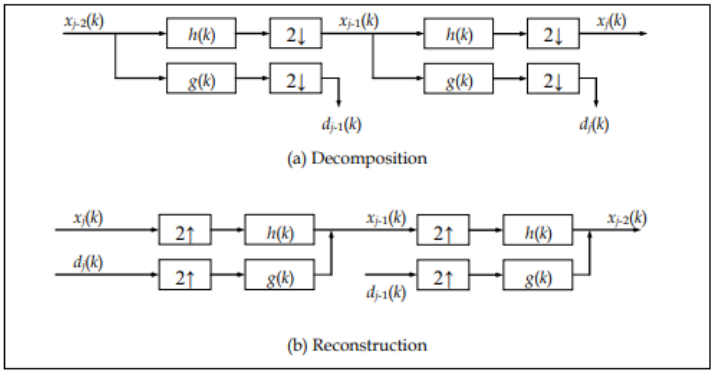

Figure 10. Implementation of DWT by using discrete filter banks.

The signal is first filtered with special lowpass $h(k)$ and highpass $g(k)$ filters to obtain lowpass and highpass sub-bands reconstructed through the definition of approximation coefficients (x_{j1}) and detail coefficients (d_{j1}), respectively. The detail coefficients are called wavelet coefficients. In the next level of decomposition, the lowpass sub-band is iteratively filtered by the same technique to yield narrower sub bands. The length of the coefficients in each sub-band is half of the number of coefficients in the preceding stage. These filters also can reconstruct the sub-bands while cancelling any aliasing that occurs due to down sampling.

The steps involved in wavelet denoising are:

1. Multilevel wavelet decomposition.
2. Choose of a suitable thresholding technique.
3. Threshold of the wavelet coefficients and reconstruct the signal: DWT is invertible, so the signal can be reconstructed from the DWT coefficients with the inverse DWT.

The analytical treatment made for the wavelet in the one-dimensional case, extends similarly to the two-dimensional case, operating first along the rows and then along the columns of the signal.

Divergence-Free Wavelet denoising inherits advantages of wavelet denoising, including efficient multiscale decompositions, edge preserving transforms, and sparse representation of signals, while amounting to only linear computational complexity.

DFW transformation projects a 3D vector field on multivariate divergence-free wavelet bases (orthogonal or biorthogonal) obtained by tensor products of one-dimensional wavelets or scaling functions. To construct the divergence-free wavelet bases one needs to start with a vector multiresolution analysis (MRA) (Erwan Deriaz, 2007).

Multi-resolution analysis are approximation spaces that allow the construction of divergence-free wavelet bases where the flow field, subjected to the divergence reduction process of velocity data, is projected. Analysing the two-dimensional case, let $\left(V_j^0\right)$ be a one-dimensional MRA with differentiable scaling function ϕ_1 and wavelet function ψ_1. Then one can be build a MRA $\left(V_j^1\right)$ with a scaling function ϕ_0 and wavelet function ψ_0, verifying:

$$V_0^0 = span\{\phi_0(x-k), \qquad k \in \mathbb{Z}\}$$
$$V_0^1 = span\{\phi_1(x-k), \qquad k \in \mathbb{Z}\}$$

and

$$\phi'_1(x) = \phi_0(x) - \phi_0(x-1) \tag{49}$$

$$\psi'_1(x) = 4\psi_0(x) \tag{50}$$

Linear and quadratic spline scaling functions ϕ_0, ϕ_1 and wavelet functions ψ_0, ψ_1 (Figure 11) satisfy the above propositions and are used to construct DFWs, by combining appropriate tensor products of these functions.

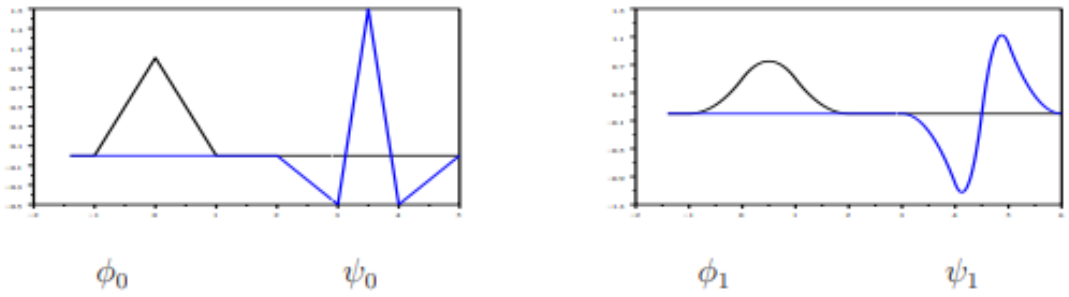

Figure 11. Representation of linear and quadratic spline scaling functions ϕ_0, ϕ_1 and wavelet functions ψ_0, ψ_1. In black: linear and quadratic spine scaling functions. In blue: linear and quadratic spline wavelet functions.

The starting point of the construction of 2D divergence-free basis wavelets lies in considering as multiresolution analysis of $L^2(\mathbb{R}^2)^2$ the vector space of tensor-products $\left(V_j^1 \otimes V_j^0\right) \times \left(V_j^0 \otimes V_j^1\right)$. In the isotropic case, the 2D scaling functions ϕ_0, ϕ_1 and wavelets ψ_0, ψ_1 of this MRA are given by:

$$\phi_1(x,y) = \begin{vmatrix} \phi_1(x)\phi_0(y) \\ 0 \end{vmatrix} \tag{51}$$

$$\phi_2(x,y) = \begin{vmatrix} 0 \\ \phi_0(x)\phi_1(y) \end{vmatrix} \tag{52}$$

$$\Psi_1^{(1,0)}(x,y) = \begin{vmatrix} \psi_1(x)\phi_0(y) \\ 0 \end{vmatrix} \tag{53}$$

$$\Psi_2^{(1,0)}(x,y) = \begin{vmatrix} 0 \\ \psi_0(x)\phi_1(y) \end{vmatrix} \tag{54}$$

$$\Psi_1^{(0,1)}(x,y) = \begin{vmatrix} \phi_1(x)\phi_0(y) \\ 0 \end{vmatrix} \tag{55}$$

$$\Psi_2^{(0,1)}(x,y) = \begin{vmatrix} 0 \\ \phi_0(x)\phi_1(y) \end{vmatrix} \tag{56}$$

$$\Psi_1^{(1,1)}(x,y) = \begin{vmatrix} \psi_1(x)\psi_0(y) \\ 0 \end{vmatrix} \tag{57}$$

$$\Psi_2^{(1,1)}(x,y) = \begin{vmatrix} 0 \\ \psi_0(x)\psi_1(y) \end{vmatrix} \tag{58}$$

Then, using the above functions, two-dimensional divergence-free scaling and wavelet functions can be constructed (Figure 12). The 2D divergence-free vector scaling functions takes the form:

$$\phi_{div}(x,y,z) = \begin{vmatrix} \phi_1(x)[\phi_0(y) - \phi_0(y-1)] \\ -[\phi_0(x) - \phi_0(x-1)]\phi_1(y) \end{vmatrix} \tag{59}$$

And the corresponding isotropic vector wavelets are given by the system:

$$\Psi_{div}^{(1,0)}(x,y) = \begin{vmatrix} -\frac{1}{4}\psi_1(x)[\phi_0(y) - \phi_0(y-1)] \\ \psi_0(x)\phi_1(y) \end{vmatrix} \tag{60}$$

$$\Psi_{div}^{(0,1)}(x,y) = \begin{vmatrix} \phi_1(x)\psi_0(y) \\ -\frac{1}{4}[\phi_0(x) - \phi_0(x-1)]\psi_1(y) \end{vmatrix} \tag{61}$$

$$\Psi_{div}^{(1,1)}(x,y) = \begin{vmatrix} \psi_1(x)\psi_0(y) \\ -\psi_0(x)\psi_1(y) \end{vmatrix} \tag{62}$$

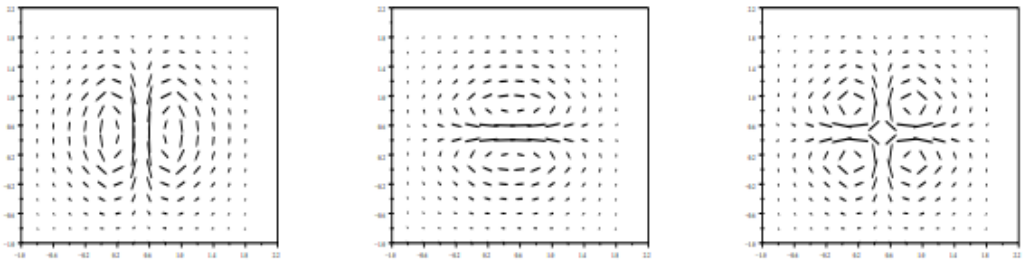

Figure 12. Representation of isotropic 2D divergence-free wavelets $\Psi_{div}^{(1,0)}$(right), $\Psi_{div}^{(0,1)}$ (centre) and $\Psi_{div}^{(1,1)}$(left).

The scaling functions generate a divergence-free MRA (Multi Resolution Analysis). In this new divergence-free MRA, one can construct isotropic as well as anisotropic divergence-free wavelet bases and its complement. The complement functions correspond to non-divergence-free part of the data (Figure 13).

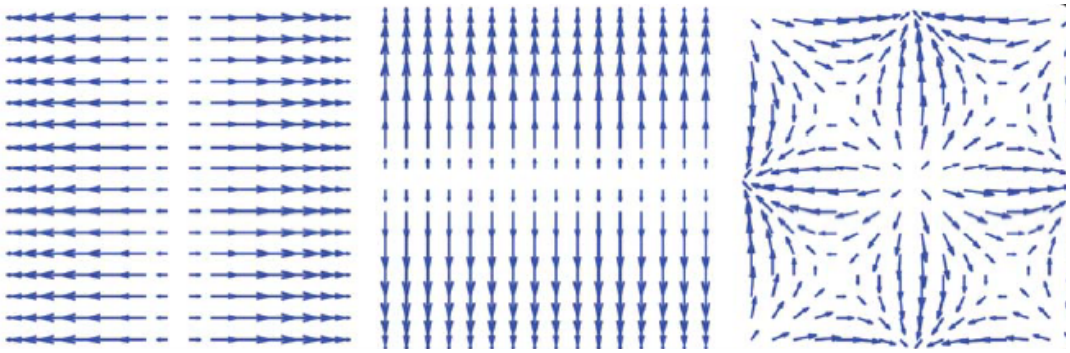

Figure 13. Representation of isotropic 2D non-divergence-free wavelets.

In the isotropic three-dimensional case, the construction of divergence-free wavelets bases starts with a vector multiresolution analysis of $L^2(\mathbb{R}^3)^3$, of the type:

$$\left[V_j = \left(V_j^1 \otimes V_j^0 \otimes V_j^0\right) \times \left(V_j^0 \otimes V_j^1 \otimes V_j^0\right) \times \left(V_j^0 \otimes V_j^0 \otimes V_j^1\right)\right]_{j \in \mathbb{Z}}$$

This MRA is constructed by three 3D vector scaling functions and a set of 21 3D vector wavelets, consisting of 14 divergence-free vector wavelets and 7 complement functions.

$$\{\Psi_i^{\varepsilon} | i = 1,2,3, \qquad \varepsilon = (\varepsilon_1, \varepsilon_2, \varepsilon_3) \; with \; \varepsilon_i = 0,1 \; and \; \varepsilon \neq (0,0,0)\}$$

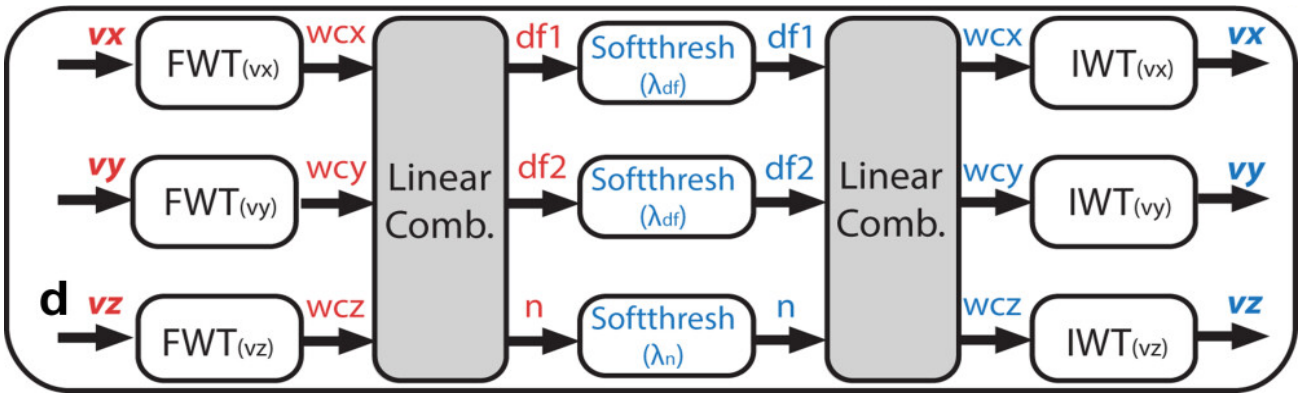

Figure 14. Flow diagram of DFW denoising.

To summarize, denoising using DFWs is performed by implementing the Discrete Wavelet Transform (or Fast Wavelet Transform), in which the transfer functions of the low-pass and high-pass filters are the linear combination of the scaling functions in one case and of the wavelet functions in the other, respectively. The coefficients obtained as output from the low-pass and high-pass filters are all that is needed to calculate the wavelet decomposition of a given function.

In denoising three-dimensional velocity data, the calculation of DFW coefficients is reduced to a linear combination of wavelet coefficients generated by the Fast Wavelet Transforms, performed separately on each velocity component (Figure 14). The complete set of linear combination equations is provided in literature (F. Ong, 2015). Resulting divergence-free and non–divergence-free coefficients, obtained from the linear combination discussed above, provide a sparse representation of the flow data, which can be, now, effectively subjected to the denoising procedure by using a soft-thresholding technique.

Denoising with DFWs allows for the preservation of flow information at the edges of segmented vessels, as a soft-thresholding threshold is chosen not only for divergence-free coefficients but also for non-divergence-free coefficients, which will not be completely eliminated. In such a manner, important flow components near the edges of the vessel will be analysed. Furthermore, to allow for better denoising performance, the threshold selected for divergence-free coefficients is separate and differs from that chosen for non-divergence-free coefficients.

SOFT-THRESHOLDING TECHNIQUE: SURESHRINK

The multilevel wavelet decomposition performed by the discrete wavelet transform, coupled with obtaining a sparse representation of the flux data, made it possible to develop a procedure with good performance in reducing the noise level superimposed on the image, while leaving its information content unchanged.

The sparsity of the signal allows the typically Gaussian noise, superimposed on the image, to be evenly distributed over all wavelet coefficients, unlike the information content of the image, which is found in a few wavelet coefficients of greater amplitude.

The denoising procedure, called SureShrink, consists of solving an optimization problem to find a threshold to subject the wavelet coefficients to the soft-thresholding procedure (Donoho DL, 1995). In the soft-thresholding procedure, coefficients with magnitude less than the threshold are set to zero, while the coefficients greater than the threshold are shrunk toward zero by subtracting the threshold value from the coefficients value.

To select an appropriate threshold for a given noise level, SureShrink is considered an optimal scheme for minimizing mean square error in the wavelet domain (Luisier F, 2007) (Fei Xiao, 2012).

It is convenient to use when the data are not sparse enough to make the use of the "universal threshold" effective. The latter is known as VisuShrink and is a function of the noise power σ^2 and of the number of signal samples N:

$$T = \sqrt{2\sigma^2 logN} \tag{63}$$

The aim of image wavelet denoising is the minimization of the estimated mean square error between the clean image and the image to be denoised, defined as follows:

$$< |\hat{x} - x|^2 \geq \sum_{j=1}^{J} \frac{N_j}{N} < \left|\hat{x}^j - x^j\right|^2 > \tag{64}$$

With SureShrink, one has the advantage of having at one's disposal a very accurate estimate of the MSE, which depends only on the noisy image and not on the clean image: Stein's Unbiased Risk Estimator (SURE). This estimate is quadratic, and its minimization is equivalent to solving a linear system of equations.

The thresholding is adaptive: a threshold is assigned to each dyadic resolution level j. For each wavelet subband J, let I_j be the index set of subband coefficients corresponding to the segmented data, N_j be the length of the index set I_j, $x_{i,j}$ be the ith subband coefficients in I_j and σ be the noise standard deviation, SureShrink chooses the subband dependent threshold t_j^* as follows:

$$t_j^* = \min_t \sigma^2 - \frac{1}{N_j}(2\sigma^2 \#\{i: |x_{i,j}| \leq t\} - \sum_{j=1}^{N_j} \min(|x_{i,j}|, t)^2) \tag{65}$$

To robustly estimate σ, median absolute deviation (MAD) was applied on the highest frequency subband of nondivergence-free component, which is given by the formula:

$$\sigma = 1.4826\, median(|x_i - median(x)|) \tag{66}$$

Thresholds for SureShrink can be computed with complexity $NlogN$.

BLOCKING ARTIFACTS: CYCLE SPINNING

Simple thresholding in an orthogonal wavelet domain can be considered as first-generation denoising: to improve its performance, SureShrink was investigated to select appropriate thresholds.

DFW denoising suffers from visual artifacts, e.g., Gibbs phenomena near discontinuities and other blocking artifacts caused by the lack of translation invariant of the wavelet basis (Donoho., 1995). To reduce such artifacts and improve denoising performance, a second-generation denoising method, named “cycle spinning” by Coifman, was considered (Vlachos., 2005).

Gibbs phenomena are caused by the fact that the reconstruction of the image with the inverse wavelet transform, after subjecting the wavelet coefficients to the soft-thresholding procedure, uses only a subset of the entire set of wavelet basis elements. Unlike the classical Gibbs phenomena associated with Fourier analysis, pseudo-Gibbs phenomena in wavelet domain are much better localized and much more moderate in their oscillations. However, they are visually displeasing and manifest as ringing in the neighbourhood of discontinuities, as alternating undershoots and overshoots of the intensity level.

The blocking artifacts are all caused by the lack of precise alignments between the signal characteristics and those of the wavelet bases.

One method to correct such misalignments is to enforce a shift to the signals, so that their features change position. Two operators, time shift (h) and frequency shift (ξ), respectively, are introduced: having chosen the best h and ξ, using an optimization algorithm, which also gives a quantitative measure of the good alignment between signal and wavelet basis, the data is shifted, denoising of the shifted data is performed, and finally the shifted data is returned to its initial position (de-shifting) during image reconstruction.

When a signal contains several discontinuities, the best shift for one discontinuity in the signal may also be the worst shift for another discontinuity. Consequently, the approach involves applying a range of shifts, and average over the several results so obtained.

Artifacts will consequently be suppressed by "medializing" the shift dependence, in a time of the order of nlog2(n).

MATERIALS AND METHODS

CFD SIMULATION

The denoising techniques were tested on synthetic velocity data obtained from a CFD simulation of hemodynamics in a realistic aorta at the systolic peak and with Gaussian noise superimposed.

First, the 3D geometry of a healthy thoracic aorta was constructed from 4D flow MRI scans through the process of segmentation and was subjected to the process of mesh generation, in order to solve the Navier-Stokes equations. Here, the blood flow is modeled as incompressible Newtonian fluid, with constant density and viscosity (density equal to $1060\ \mathrm{kg\ m^{-3}}$; dynamic viscosity equal to $3.5\ 10^{-3}\mathrm{Pa\ s}$).

The general Navier-Stokes equations for fluid motion can be written as:

$$\rho\left(\frac{\partial \mathrm{v}}{\partial \mathrm{t}} + \mathrm{v}\cdot\nabla\mathrm{v}\right) = -\nabla\mathrm{p} + \mu\Delta\mathrm{v} \tag{67}$$

Furthermore, incompressible flow must satisfy the continuity equation, formulated as:

$$\nabla\cdot\mathrm{v} = 0 \tag{68}$$

Where ρ is the fluid density, v represents the velocity vector in all three spatial directions, t is the time, ∇ is the gradient operator, p is the pressure, μ is the viscosity and Δ is the Laplacian operator.

The numerical approximation of the exact solution is accomplished by defining certain boundary conditions (BCs). Measured 3D phase-contrast flow maps were extracted along the cardiac cycle and used to generate Dirichlet inflow BCs, applied in terms of 3D velocity profiles (BC3D) at the ascending aorta (AAo) inlet section (as detailed in Morbiducci et al., 2013 and De Nisco et al., 2018). The outflow fractions from each outlet are quantified according to predefined percentages of the total outflow derived from experimental values in the literature.
Furthermore, the no slip-boundary condition, i. e., flow speed is zero at the vessel wall, is assumed.

ALGORITHM IMPLEMENTATION

The methods previously discussed, the Finite Difference Method (FDM), the Radial Basis Functions-based method (RBFs), the Divergence-Free Wavelets- based method (DFW) and finally the Divergence-Free Wavelets- based method (DFW) with the implementation of cycle spinning, were implemented using C and CUDA programming languages with MATLAB (The MathWorks, Natick, MA, USA), call into use through the mex function, on standard computer hardware.

To evaluate the reduction in divergence of velocity data, the algorithms were tested on synthetic velocity data obtained from a CFD simulation of the aorta at the systolic peak. The CFD model of the aorta was voxelized using a resolution of 0.003 m in all three directions of space. To evaluate the denoising performance of the 4 algorithms, to the synthetic reference velocity data, after being voxelized, was homogeneously distributed zero mean Gaussian noise, separately, on each direction of the 3D velocity field, in order to increase the divergence of the reference velocity field, obtained from the CFD simulation, and so, to better appreciate the denoising performance of the various algorithms. The magnitude 4D flow MRI data were used for segmentation in the CFD simulation, with SNR=14.18 dB. Since the standard deviation of the measurable velocity is proportional to the SNR and Venc, i.e. the maximum measurable velocity without incurring velocity aliasing, the latter was chosen to be 150 cm/s, a value compatible with the typical physiological velocity within the aorta.

$$\sigma = \frac{\sqrt{2}V_{enc}}{\pi\, SNR} \tag{69}$$

Starting from one of the three velocity components (u, v or w) in the parallelepiped representing the FOV (30x45x16), the binary mask (imMag), useful for vessel segmentation (imMask), was derived, setting non-zero velocity values equal to 1, being the velocity in the voxels outside the vessel already zero.

In order to assess the robustness of the algorithms FDM, RBFs – based method, DFW – based method with SureShrink and MAD estimation of noise and DFWs – based method with partial cycle spinning were implemented in MATLAB for comparison, on noisy velocity data.

For FDM denoising, first-order finite difference and periodic boundary conditions were used.

For RBF denoising, matrix valued RBF based on the Gaussian function, for each spatial point, was generated and it was used as convolution kernel for a given radius. The support of the basis functions (2*radius+1, 2*radius+1, 2*radius+1) was set to be (9,9,9; radius=4) as they produced low errors. A binary certainty function with a uniform non-zero weight for flow regions was used for normalized convolution for RBF, providing an optimal balance between smoothness and local approximation of the velocity vector field. Iterative least squares in RBF were implemented with LSQR (27) in MATLAB with maximum number of iterations set to (100). The values radius=4 and Niter=100 were selected based on a not in-depth sensitivity analysis, based only on the quantitative parameters of the error in restoring the reference velocity fields.

For the construction of the Divergence-Free Wavelet (DFW), linear spline wavelets were utilized for ϕ_0 and ψ_0, while quadratic spline wavelets were employed for ϕ_1 and ψ_1, all incorporating symmetric boundary extensions. Unless otherwise specified, two levels of wavelet decompositions were used for CFD simulations.

To simplify the process, partial cycle spinning was implemented instead of the full cycle spinning. This method involves randomly shifting the input data, applying DFW denoising, and averaging the results over a few iterations. In all experiments, eight random shifts were used for partial cycle spinning. During the soft-thresholding operation, the wavelet coefficients at the coarsest level remained unchanged since they were not sparse. For threshold selection, SureShrink and Median Absolute Deviation (MAD) were used unless stated otherwise. Specifically, for SureShrink, MAD was applied to the highest frequency subband of the nondivergence-free component to estimate the noise standard deviation, as this approach provides more accurate estimates when applied to a sparser subband.

The algorithms that have been implemented are available in a software package provided by Ong et al. (F. Ong, 2015), to reproduce some of the results obtained in their publication, reported in the literature. The software can be downloaded from:

http://www.eecs.berkeley.edu/~mlustig/Software.html.

ParaView software was used for better visualization of flow in 3D, in absence and presence of noise, and to calculate and visually assess divergence decrease.

ERROR MEASURING PARAMETERS

For a quantitative analysis of the results, denoising performances were quantified through an error analysis of the flow data processed with the denoising algorithms, compared with the original flow data, taken as a reference.

More specifically, let N be the number of segmented voxels and $V_{i,ref}$ and $V_{i,denoised}$ be the reference and denoised velocity vectors, respectively, at the i^{th} segmented voxel, so, each denoising performance was quantified with regard to the following parameters:

$Velocity\ NRMSE$ ($vNRMSE$): computes the root mean square deviation between the reference and the denoised velocity fields. It measures how well a denoising or smoothing technique has retained the original velocity characteristics (both in terms of direction and magnitude).

$$Velocity\ NRMSE = \frac{1}{max_i(|\boldsymbol{V_{i,ref}}|)} \sqrt{\frac{1}{N}\sum_{i=0}^{N} |\boldsymbol{V_{i,ref}} - \boldsymbol{V_{i,denoised}}|^2} \tag{70}$$

$Speed\ NRMSE$ (sNRMSE): computes the root mean square deviation between the magnitude of the reference and that of the denoised velocity fields. It measures how well a denoising or smoothing technique has retained the original velocity characteristics (only in terms of magnitude).

$$Speed\ NRMSE = \frac{1}{max_i(|\boldsymbol{V_{i,ref}}|)} \sqrt{\frac{1}{N}\sum_{i=1}^{N} \left(|\boldsymbol{V_{i,ref}}| - |\boldsymbol{V_{i,denoised}}|\right)^2} \tag{71}$$

$Absolute\ Error\ in\ Flow\ Direction$ (AEFD): compares the alignment between the reference velocity field and the denoised one.

$$Absolute\ Error\ in\ Flow\ Direction = \frac{1}{N}\sum_{i=1}^{N} \left(1 - \frac{|\boldsymbol{V_{i,ref}} \cdot \boldsymbol{V_{i,denoised}}|}{|\boldsymbol{V_{i,ref}}||\boldsymbol{V_{i,denoised}}|}\right) \tag{72}$$

$Alignment\ Similarity\ Index$ (ASI): measures the degree of alignment between the reference velocity field and the denoised one (both in terms of direction and magnitude).

$$Alignment\ Similarity\ Index \triangleq \frac{1}{2}\left(1 + \frac{\boldsymbol{V}_{i,denoised} \cdot \boldsymbol{V}_{i,ref}}{\left|\boldsymbol{V}_{i,denoised}\right|\left|\boldsymbol{V}_{i,ref}\right|}\right) \tag{73}$$

$Magnitude\ Similarity\ Index$ (MSI): measures the degree of alignment between the reference velocity field and the denoised one (only in terms of magnitude).

$$Magnitude\ Similarity\ Index \triangleq 1 - \left|\frac{\left|\boldsymbol{V}_{i,denoised}\right|}{\max\left(\left|\boldsymbol{V}_{i,denoised}\right|\right)} - \frac{\left|\boldsymbol{V}_{i,ref}\right|}{\max\left(\left|\boldsymbol{V}_{i,ref}\right|\right)}\right| \tag{74}$$

$Similarity\ Index$ (SI): synthesizes information derived from both ASI and MSI into a single measure.

$$Similarity\ Index = ASI * MSI \tag{75}$$

The denoising performance is better the more the first three mentioned error measurement parameters (vNRMSE, sNRMSE, AEFD) are close to zero and the more ASI, MSI and SI are close to 1, reflecting a perfect alignment between the simulated hemodynamic flow conditions before and after the denoising operation.

Furthermore, scatter plot of velocity magnitude distributions are used to better understand quantitative data, while violin plots are used for comparing probability distributions of divergence data.

RESULTS

The performances of the four denoising algorithms were qualitatively compared through visualization of (i) the original synthetic 3D blood velocity field (obtained after the voxelization of CFD data and therefore considered as the ground truth), (ii) the noisy synthetic 3D blood velocity field (obtained after the voxelization and the noise superimposition on the CFD data), and (iii) the denoised synthetic 3D blood velocity field. The same qualitative approach was used to compare divergence reduction performances.

The velocity vectors distribution of the original synthetic flow field shows, at the systolic peak, a high-speed flow region with maximum velocity at the inner lateral side of ascending aorta and near the aortic arch. In the descending aorta, a homogeneous velocity both in magnitude and direction is observed, which decreases and becomes close to zero near the vessel walls, in agreement with the no-sleep boundary condition at the vessel walls.

Superimposing the white Gaussian noise on the CFD-simulated flow results in slightly higher velocities in magnitude. Furthermore, as can be seen from the images in which the original and noisy velocity fields are superimposed (Figure 19-22), the noisy velocity vector field will undergo changes in the direction of the velocity vectors, particularly at the ascending aorta, the aortic arch and near the vessel walls.

In both cases the higher velocity is in correspondence of the inlet of the supra-aortic vessels.

To verify the correctness and accuracy of the restoration of the original velocity distribution after the denoising procedure, the simulated flow within a realistic aorta with superimposed noise was processed by 4 different approaches.

The FDM method (Figure 15) reconstructs the original velocity field with many errors, both in magnitude and direction. It is an approach sensitive to segmentation errors, which confuses the geometric model of the realistic aorta with the (synthetic) background tissues. This involves over-segmentation of regions where the velocity field should not be reconstructed, leading to detection of erroneous and insignificant details.

The projective technique using RBFs and normalized convolution (Figure 16) performs significantly better than the FDM method: the flow field is completely reconstructed, comparable to the original, in the vessel lumen. Instead, the velocities near the vessel walls aren’t fully restored as the originals. Despite the use of the binary certainty function the approach remains sensitive to segmentation errors.

The best performance, in reconstructing the original flow field, is achieved with divergence free wavelets (Figure 17): a sparse representation of the flow is obtained and the velocity components near the edges of the vessel are also reconstructed correctly. The performance is higher if partial cycle spinning is used (Figure 18).

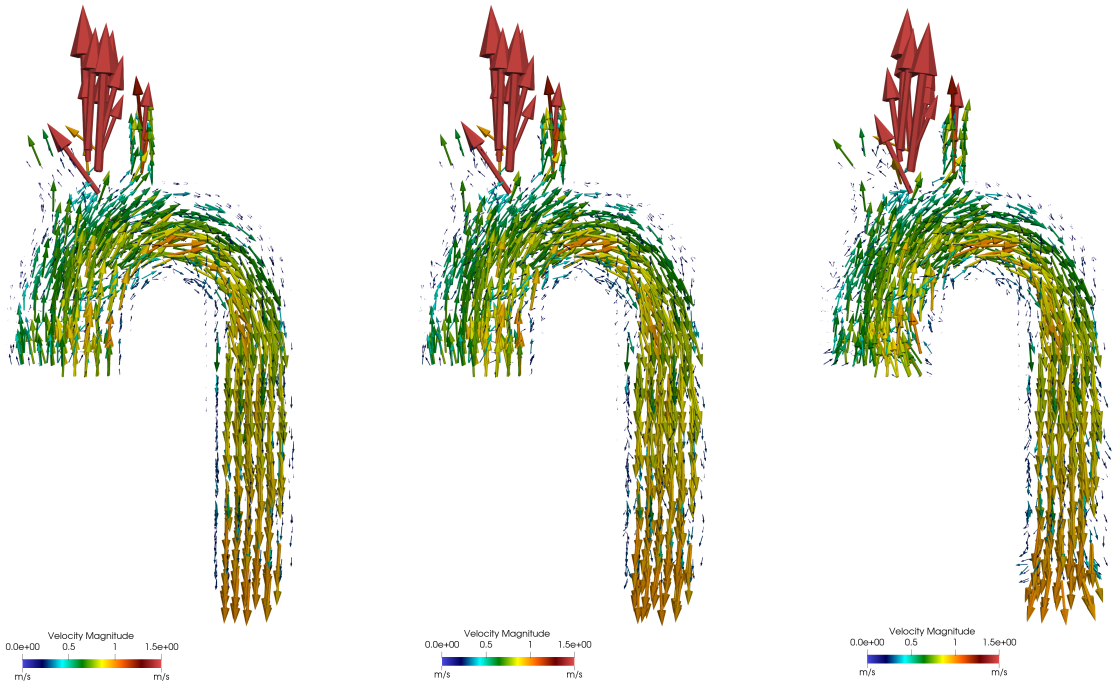

Figure 15. Comparison between, from left to right: synthetic original velocity field, synthetic velocity field with superimposed Gaussian noise, synthetic velocity field subjected to the denoising procedure with FDM.

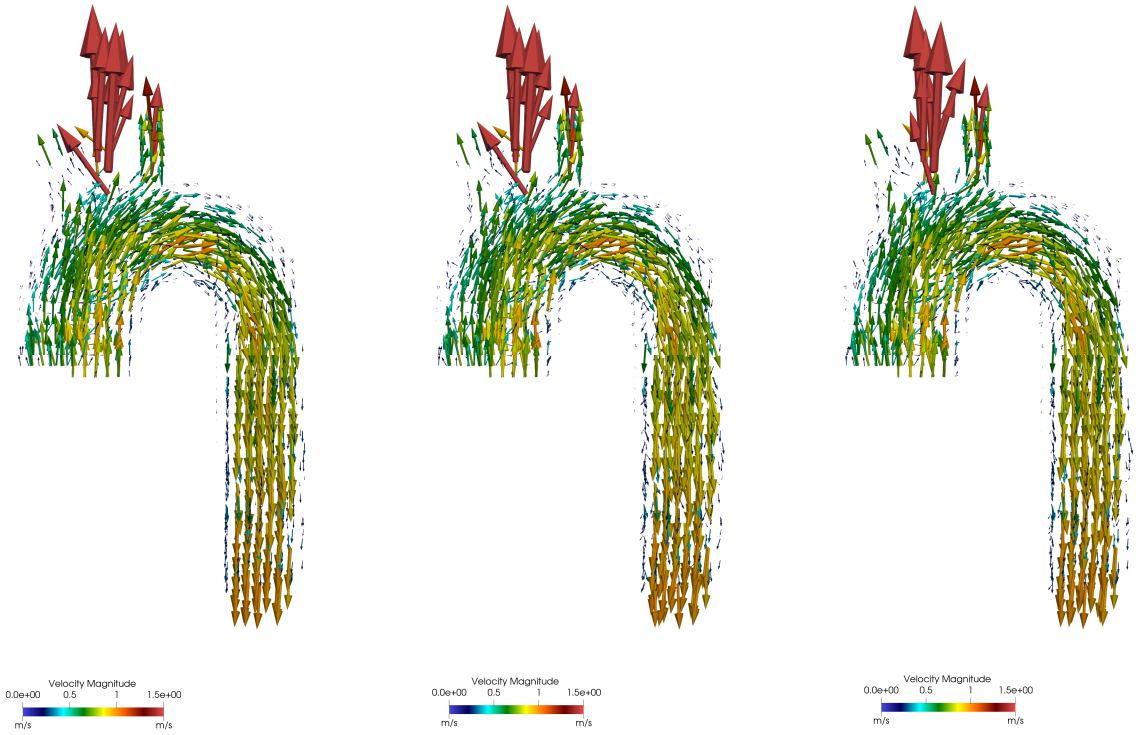

Figure 16. Comparison between, from left to right: synthetic original velocity field, synthetic velocity field with superimposed Gaussian noise, synthetic velocity field subjected to the denoising procedure with projection into RBFs.

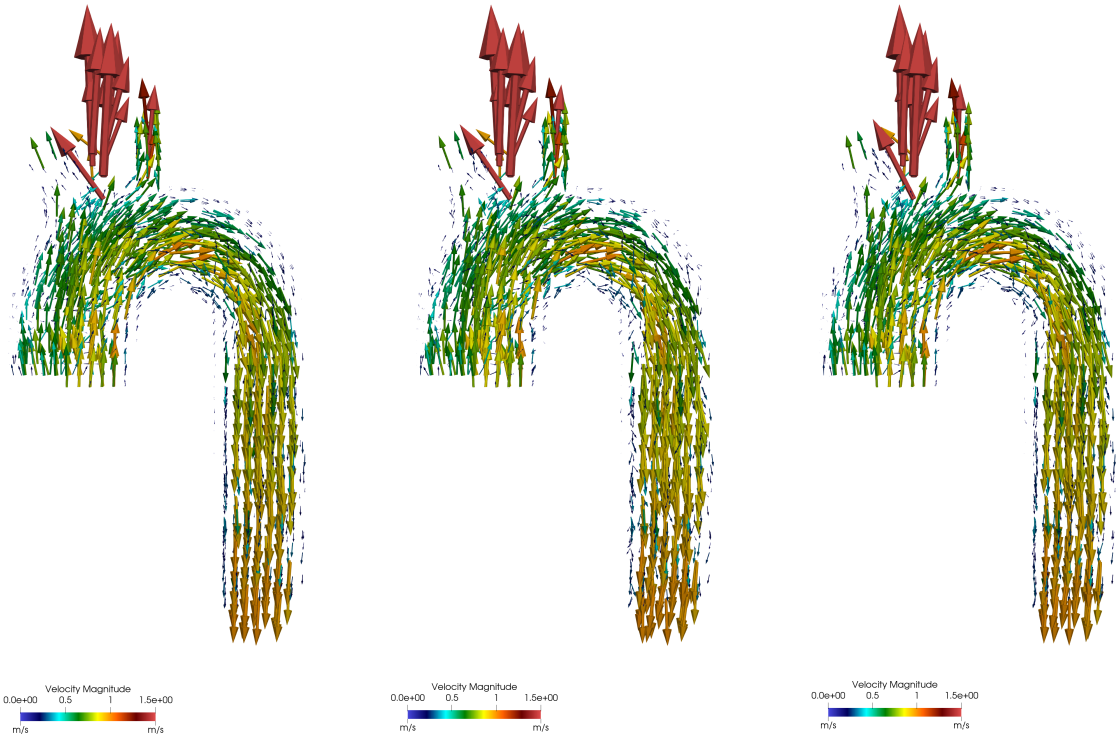

Figure 17. Comparison between, from left to right: synthetic original velocity field, synthetic velocity field with superimposed Gaussian noise, synthetic velocity field subjected to the denoising procedure with DFWs.

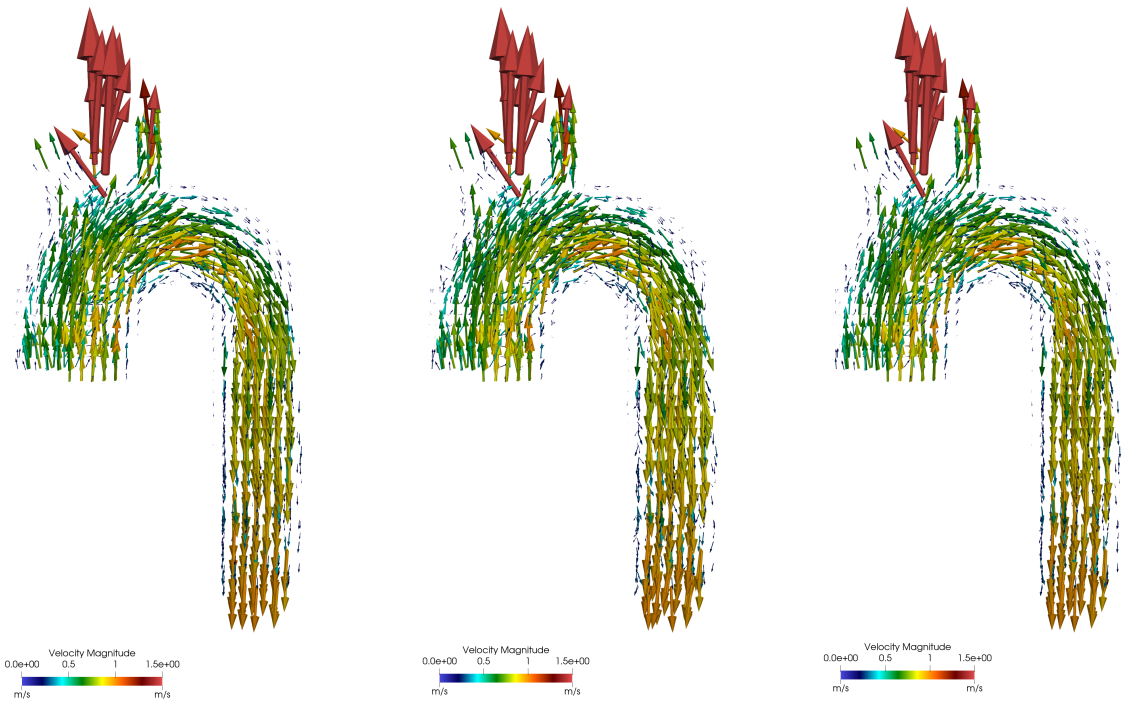

Figure 18. Comparison between, from left to right: synthetic original velocity field, synthetic velocity field with superimposed Gaussian noise, synthetic velocity field subjected to the denoising procedure with DFWs and partial cycle spinning.

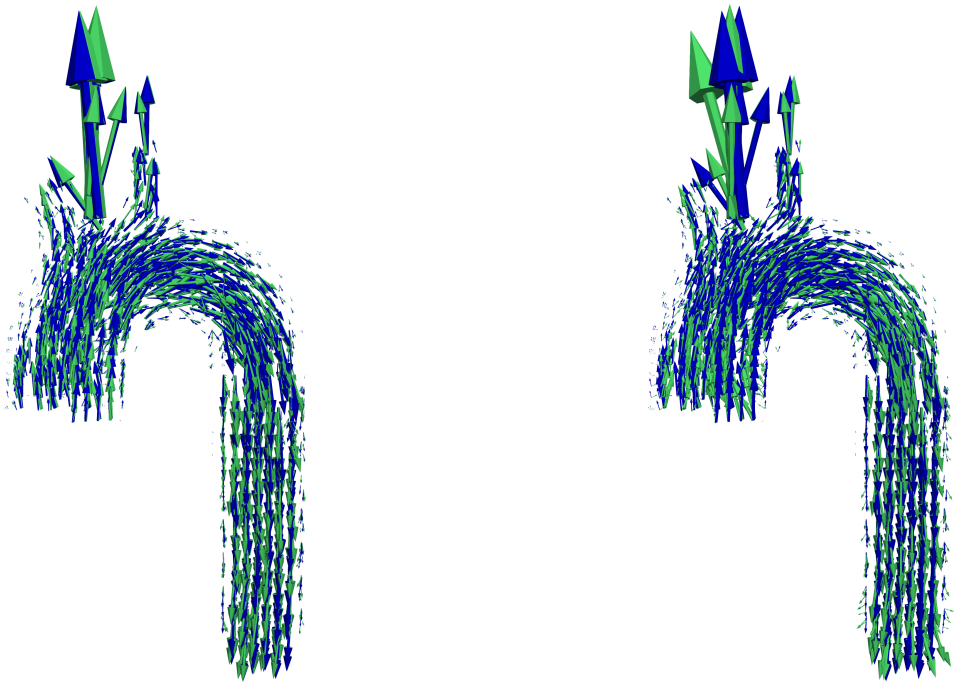

Figure 19. Comparison between, from left to right: “original” and “noisy” velocity fields overlapped with two different colors (original in blue and noisy in green), “original” and “denoised with FDM” velocity fields overlapped with two different colors (original in blue and denoised in green).

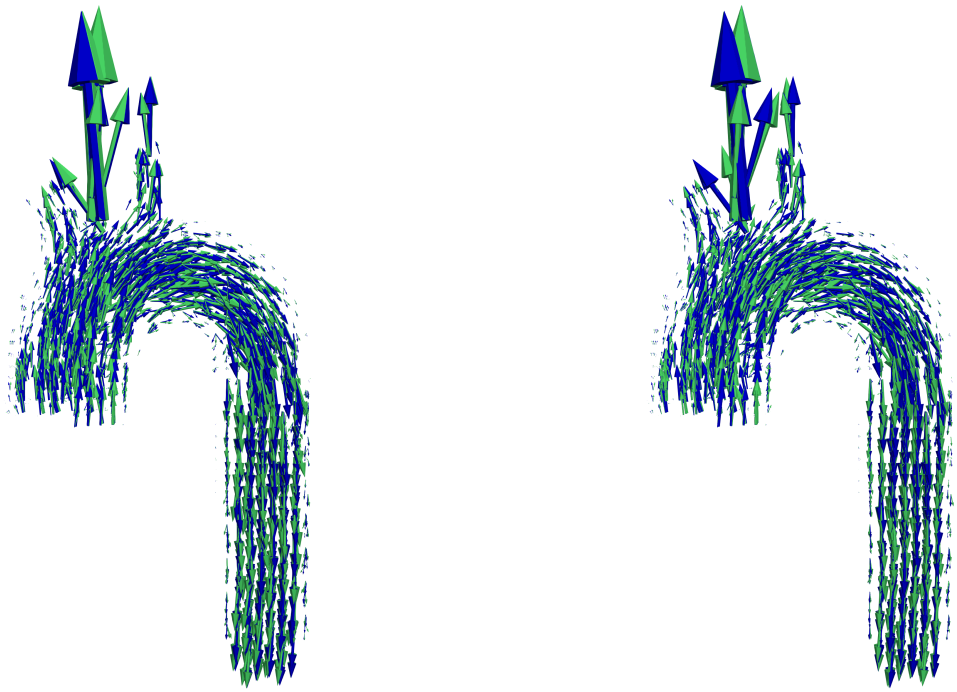

Figure 20. Comparison between, from left to right: “original” and “noisy” velocity fields overlapped with two different colors (original in blue and noisy in green), “original” and “denoised with RBFs” velocity fields overlapped with two different colors (original in blue and denoised in green).

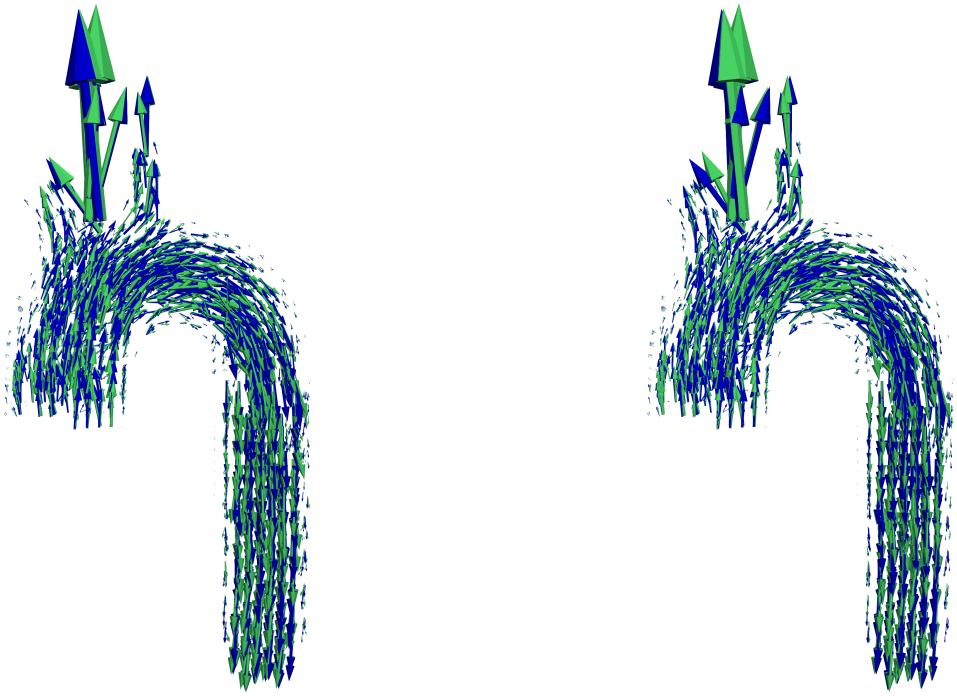

Figure 21. Comparison between, from left to right: “original” and “noisy” velocity fields overlapped with two different colors (original in blue and noisy in green), “original” and “denoised with DFWs” velocity fields overlapped with two different colors (original in blue and denoised in green).

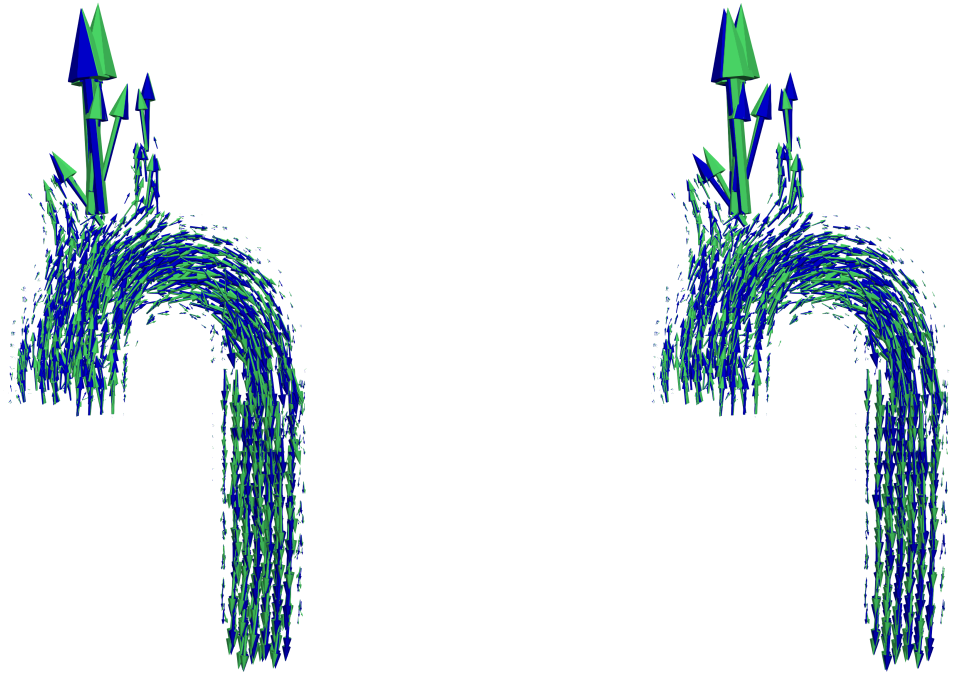

Figure 22. Comparison between, from left to right: “original” and “noisy” velocity fields overlapped with two different colors (original in blue and noisy in green), “original” and “denoised with DFWs and partial cycle spinning” velocity fields overlapped with two different colors (original in blue and denoised in green).

Furthermore, to evaluate the performances of the denoising algorithms, not only the restoration of the original flow field but also the reduction of divergence on two-dimensional slices of the realistic aorta was qualitatively analyzed, by comparing the divergence of the original velocity field, that of the noisy velocity field and that of the noisy velocity field subjected to each of the denoising procedures.

Within the aorta, velocity divergence values of the original flow field are highest at the branching points where blood flow splits into multiple arteries. This phenomenon is particularly evident near the aortic arch, where the aorta branches into supra-aortic arteries supplying blood to the head and upper limbs. Divergence takes higher values in the synthetic flow model with Gaussian noise superimposed.

After applying the algorithm which use finite differences (FDM), a reduction in divergence components was visually observed (Figure 23), which appear to be smoother but distributed like those in the noisy model. On the cross-sections of the ascending aorta, the divergence obtained with FDM appears to be lower than that in the original flow. There is a risk of missing flow patterns that might be relevant.

With the RBFs-based method (Figure 24), a soft smoothing effect on divergence of the noisy flow field is visually observed following the denoising process. This soft smoothing effect may cause fluid dynamic patterns of interest to be overlooked. However, this issue can potentially be mitigated by increasing the kernel size, but this would lead to deviation from the original flow field.

Applying the DFW-based method the divergence is reduced and more closely aligns with that of the original data (Figure 25-26): some divergence values of the original flow field, especially those at the aortic arch, are preserved, compared to the original synthetic flow data.

The same qualitative considerations are applicable to the calculation of divergence on the cross-sections of ascending and descending aorta.

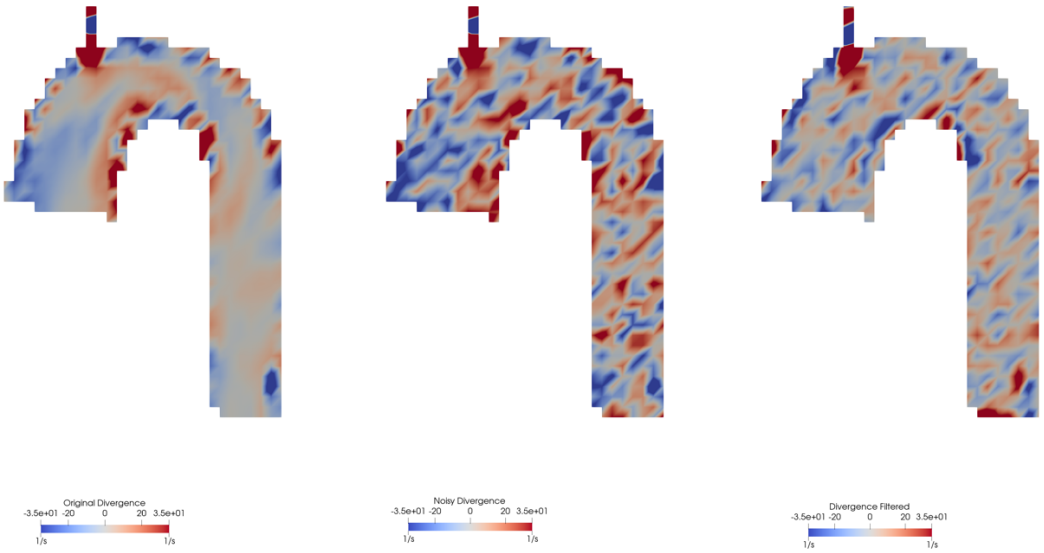

Figure 23. Comparison between the divergence in a bidimensional slice of the realistic aorta, which arise, respectively, from left to right, in original synthetic velocity field, synthetic velocity field with superimposed Gaussian noise, synthetic noisy velocity field subjected to the denoising procedure with FDM.

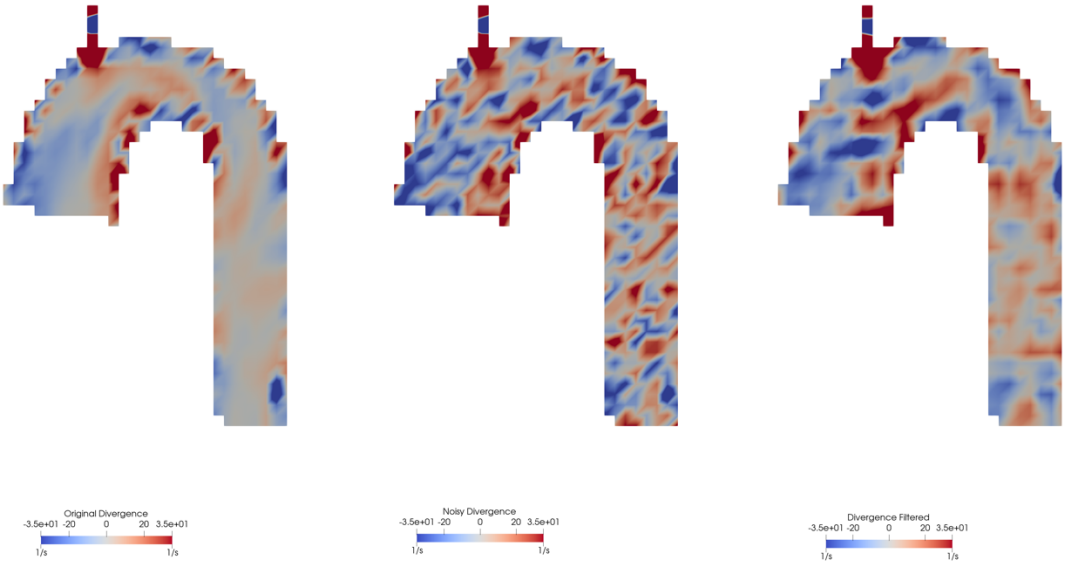

Figure 24. Comparison between the divergence in a bidimensional slice of the realistic aorta, which arise, respectively, from left to right, in original synthetic velocity field, synthetic velocity field with superimposed Gaussian noise, synthetic noisy velocity field subjected to the denoising procedure with projection into RBFs.

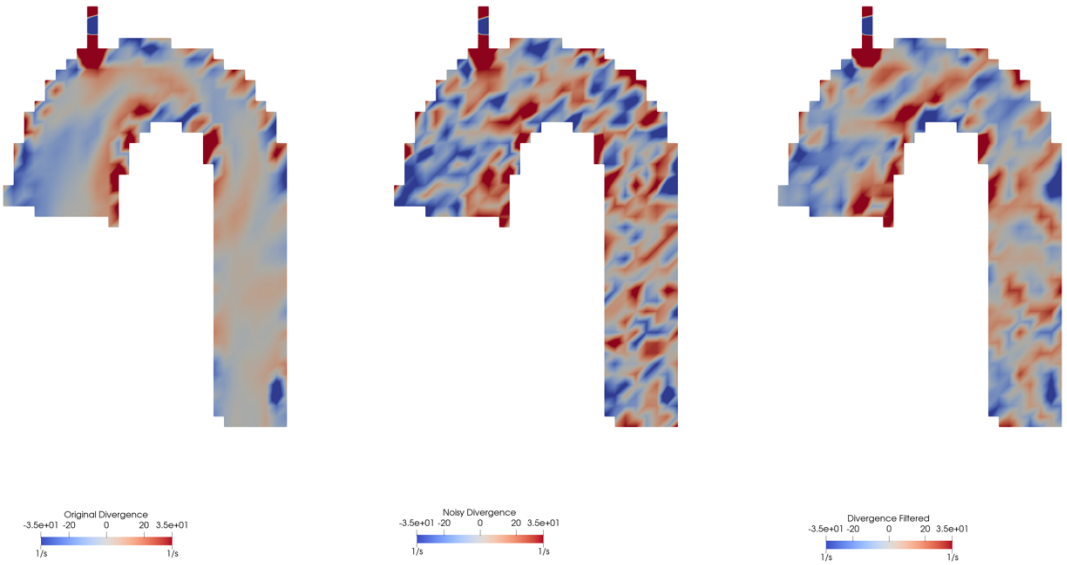

Figure 25. Comparison between the divergence in a bidimensional slice of the realistic aorta, which arise, respectively, from left to right, in original synthetic velocity field, synthetic velocity field with superimposed Gaussian noise, synthetic noisy velocity field subjected to the denoising procedure with DFWs.

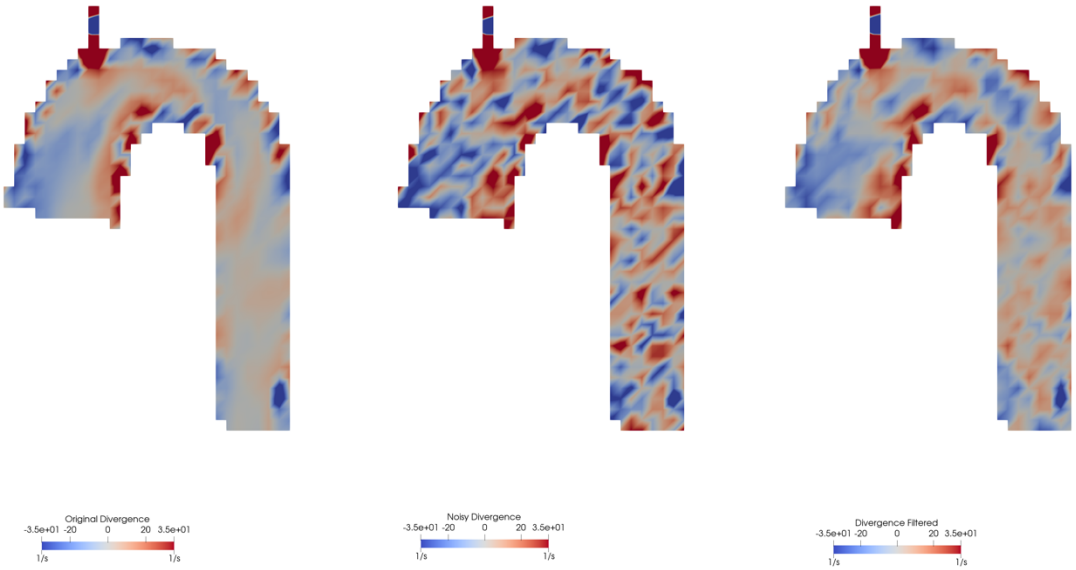

Figure 26. Comparison between the divergence in a bidimensional slice of the realistic aorta, which arise, respectively, from left to right, in original synthetic velocity field, synthetic velocity field with superimposed Gaussian noise, synthetic noisy velocity field subjected to the denoising procedure with DFWs and partial cycle spinning.

The following tables collect the values of each of the parameters discussed in the section Error Analysis for each of the 4 approaches used for denoising.

	Finite Difference Method	Radial Basis Functions (nIter=100; radius=4)	DivFree Wavelet w/ SureShrink and MAD	DivFree Wavelet w/ SureShrink, MAD and Partial Cycle Spinning
vNRMSE	0.034097	0.020647	0.014279	0.011147
sNRMSE	0.022624	0.016892	0.010723	0.008750
AEFD	0.106838	0.049448	0.029426	0.019452

Table 3. Values of vNRMSE, sNRMSE, AEFD for each of the denoising methods.

ASI	Finite Difference Method Error	Radial Basis Function Error (nIter=100; radius=4)	DivFree Wavelet w/ SureShrink and MAD	DivFree Wavelet w/ SureShrink, MAD and Partial Cycle Spinning
Mean	0.9314	0.9691	0.9812	0.9889
Median	0.9911	0.9983	0.9986	0.9993
25° percentile	0.9501	0.99	0.9935	0.9966
75° percentile	0.9977	0.9995	0.9996	0.9998

Table 4. Mean, median, 25° percentile, 75° percentile of ASI for each of the denoising methods.

MSI	Finite Difference Method Error	Radial Basis Function Error (nIter=100; radius=4)	DivFree Wavelet w/ SureShrink and MAD	DivFree Wavelet w/ SureShrink, MAD and Partial Cycle Spinning
Mean	0.9702	0.9856	0.9916	0.9926
Median	0.9738	0.9878	0.9930	0.9938
25° percentile	0.9564	0.9799	0.9879	0.9896
75° percentile	0.9876	0.9943	0.9968	0.9972

Table 5. Mean, median, 25° percentile, 75° percentile of MSI for each of the denoising methods.

SI	Finite Difference Method Error	Radial Basis Function Error (nIter=100; radius=4)	DivFree Wavelet w/ SureShrink and MAD	DivFree Wavelet w/ SureShrink, MAD and Partial Cycle Spinning
Mean	0.9030	0.9550	0.9728	0.9816
Median	0.9496	0.9804	0.9885	0.9909
25° percentile	0.9213	0.9665	0.9796	0.985
75° percentile	0.9672	0.9893	0.9943	0.9952

Table 6. Mean, median, 25° percentile, 75° percentile of SI for each of the denoising methods.

The quantitative analysis above shows better performance in denoising with DFW-based method with partial cycle spinning: values of $vNRMSE$, $sNRMSE$ and $AEFD$ (Table 3) are closer to zero, and values of *ASI, MSI* and *SI* (Table 4-6) are closer to 1. Quantitatively, velocity NRMSE, speed NRMSE, and direction error for the denoised flow with DFW with cycle spinning are respectively 0.0112, 0.0088 and 0.0195. DFW with cycle spinning achieves the lowest errors in all three error criteria. At the same time, it achieves the higher mean value of ASI, MSI and SI, respectively 0.9886, 0.9928, 0.9815. This means a very good similarity between reference hemodynamic conditions and the denoised ones, more than other denoising strategies, in performance order: DFW without partial cycle spinning, RBFs based method and FDM.

The following scatter represents the relationship between the magnitude of the velocity of the original synthetic flow data and the magnitude of the velocity of the synthetic denoised flow data, for each of the denoising procedures. The red line indicates the perfect match line among the original velocity magnitude and the filtered velocity magnitude, while the green line is the regression line of the two sets of velocity magnitude data. In the legend the Pearson's coefficient (r) is shown, as a measure of the linear correlation between the two velocity magnitude data.

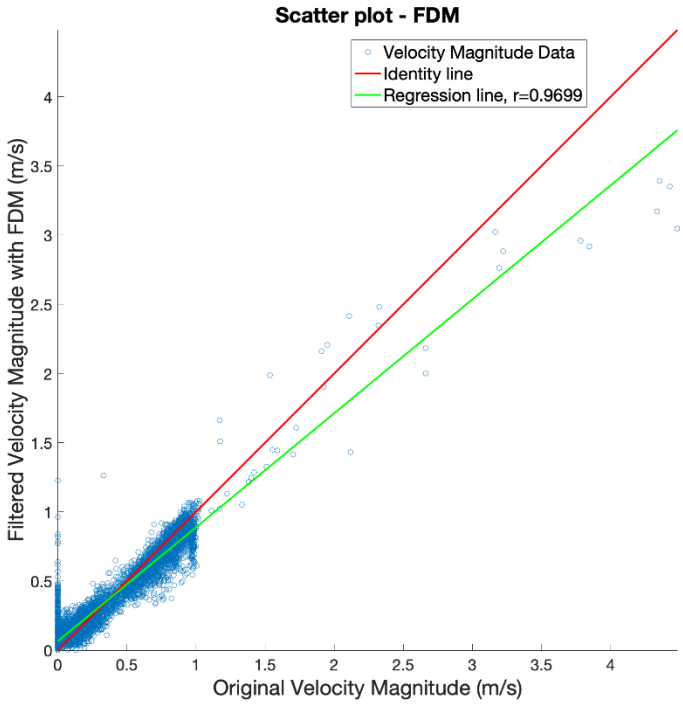

Figure 27. Plot of velocity magnitude distributions as a scatter plot: filtered velocity magnitude with FDM vs. original velocity magnitude.

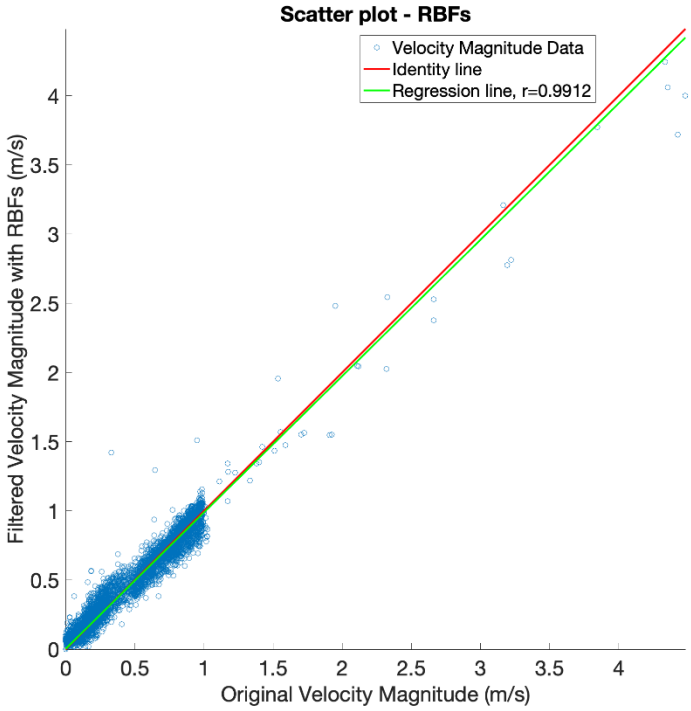

Figure 28. Plot of velocity magnitude distributions as a scatter plot: filtered velocity magnitude with projection into RBFs vs. original velocity magnitude.

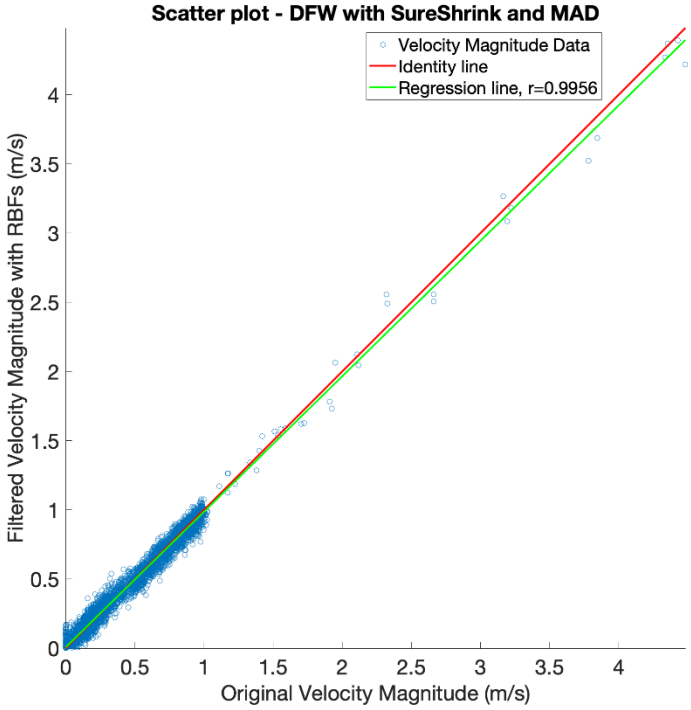

Figure 29. Plot of velocity magnitude distributions as a scatter plot: filtered velocity magnitude with DFW-based method vs. original velocity magnitude.

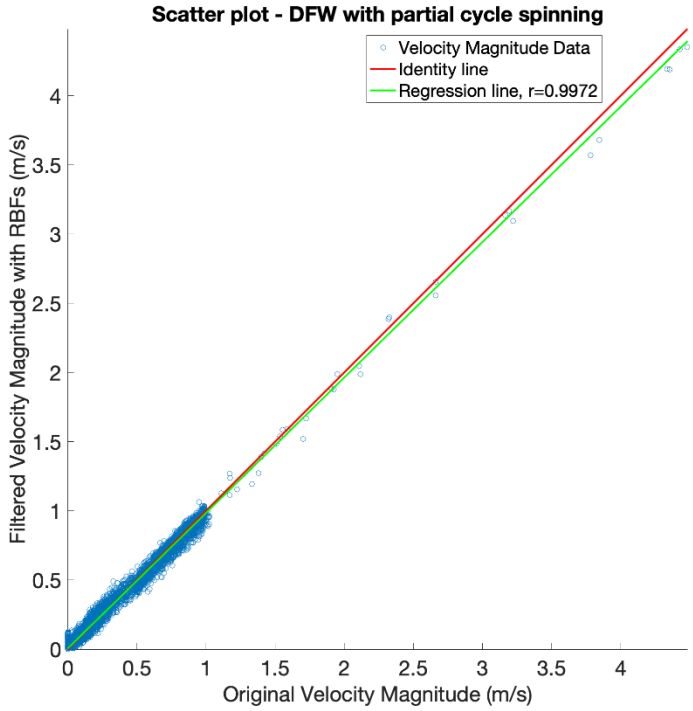

Figure 30. Plot of velocity magnitude distributions as a scatter plot: filtered velocity magnitude with DFW-based method and partial cycle spinning vs. original velocity magnitude.

The scatter plots related to the denoising methods have been reported in order of progressively better performance. FDM is the least accurate method in preserving the relationship between the original and filtered velocity data (Figure 27); this is observed by a greater dispersion of the data around the red line representing the identity line and by the regression line, the green line, deviating the most from the bisector. The correlation coefficient (Pearson) r is the lowest and is equal to 0.9699 ($p<0.05$), a value close to 1 which, however, indicates a linear correlation between the two data sets. In addition, some points outside the main lines can be seen, particularly at near-zero and higher velocity values (over 1.5 m/s). These outliers represent points where the filtered velocity does not perfectly match the original velocity, causing filtering errors and residual noise.

The RBFs method seems to be more accurate in preserving the relationship between original and filtered velocity than FDM, with slightly better correlation ($r=0.9912$; $p<0.05$) and fewer outliers (Figure 28), which are less pronounced than in the FDM plot. Although there are still some points away from the identity line, their amount and deviation from the identity line are lower, suggesting that RBFs-based method handles these values better.

The presence of a well-fitting regression line to the data and a high correlation coefficient ($r=0.9972$; $p<0.05$) suggest that the best method used to filter the data, which preserves velocity information well enough, is the DFW-based method with partial cycle spinning (Figure 30). The Pearson coefficient value is higher than that obtained with DFW-based method without partial cycle spinning (Figure 29) (0.9972 vs. 0.9956), with RBFs based-method (0.9972 vs. 0.9912) and much higher than that obtained with FDM (0.9972 vs. 0.9699). This is indicative of an almost perfect correlation and a better fit to the original values. The distribution of points is predominantly close to the identity line. Ideally, if the

data followed this line perfectly, it would mean that the filtering method introduced no distortion or change in the magnitude of the original velocity, restoring it completely.

Outliers are also present to a lesser amount, almost completely absent, demonstrating the good denoising capabilities of the methods that allow for a sparse representation of the flow field.

To quantitatively assess the performances of the algorithms in terms of divergence minimization, the probability density functions of the absolute value of divergence were computed and visualized using violin plots (Figure 31-34). The width of the violin plot, at a certain level, represents the probability density of the absolute value of divergence data at that value, that is, how concentrated the data are in that region. To quantitatively state that the denoising strategies have effectively reduced the divergence, one wants lower values of mean and median of the distributions.

The DFW-based method with partial cycle spinning is confirmed the best performing method.

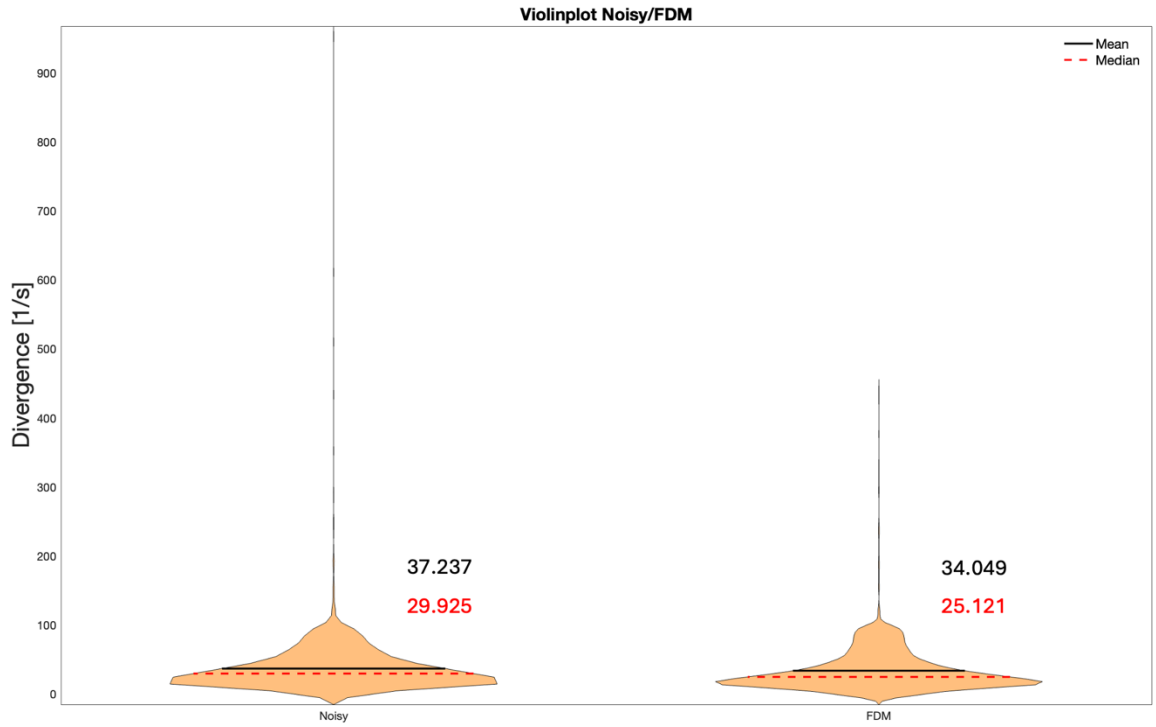

Figure 31. Plot of absolute value of divergence in a violin plot: on the left noisy divergence probability density distribution, on the right divergence probability density distribution of filtered data with FDM.

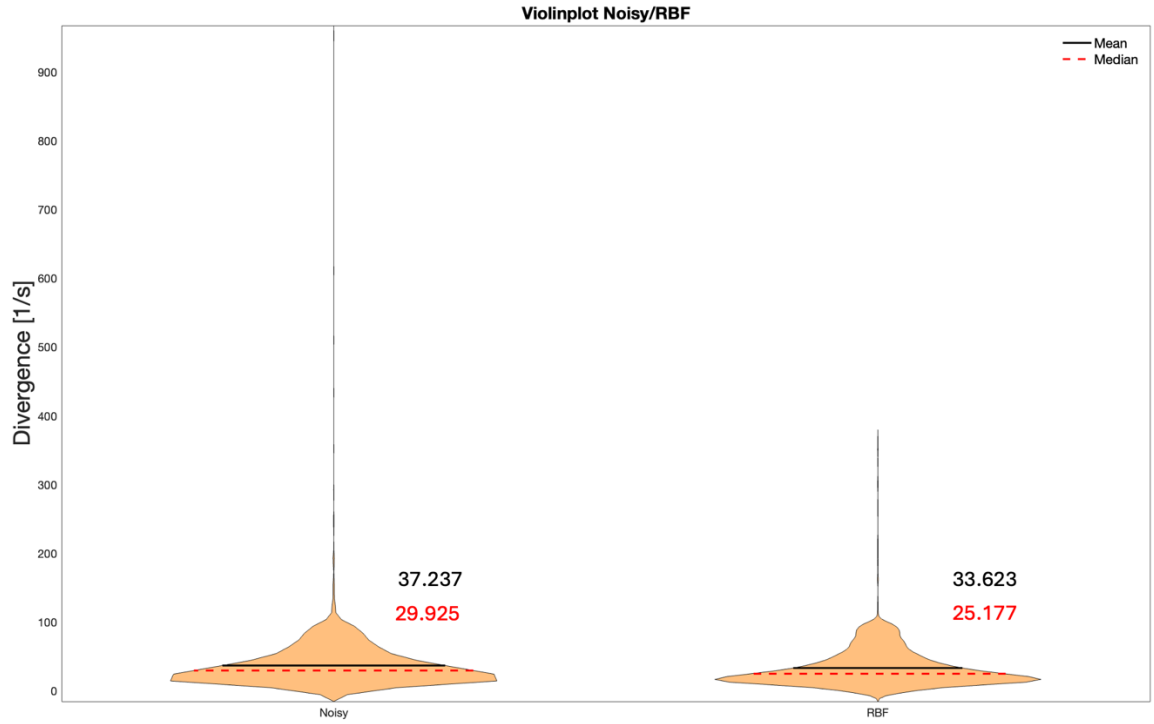

Figure 32. Plot of absolute value of divergence in a violin plot: on the left noisy divergence probability density distribution, on the right divergence probability density distribution of filtered data with RBFs.

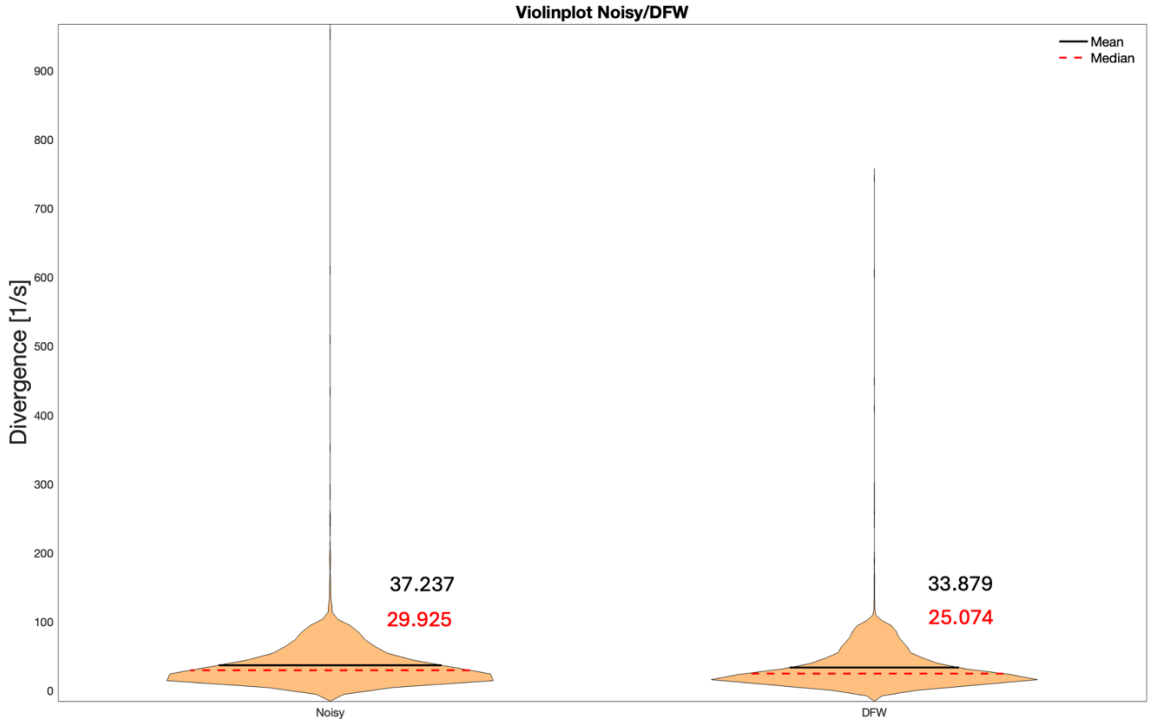

Figure 33. Plot of absolute value of divergence in a violin plot: on the left noisy divergence probability density distribution, on the right divergence probability density distribution of filtered data with DFW-based method.

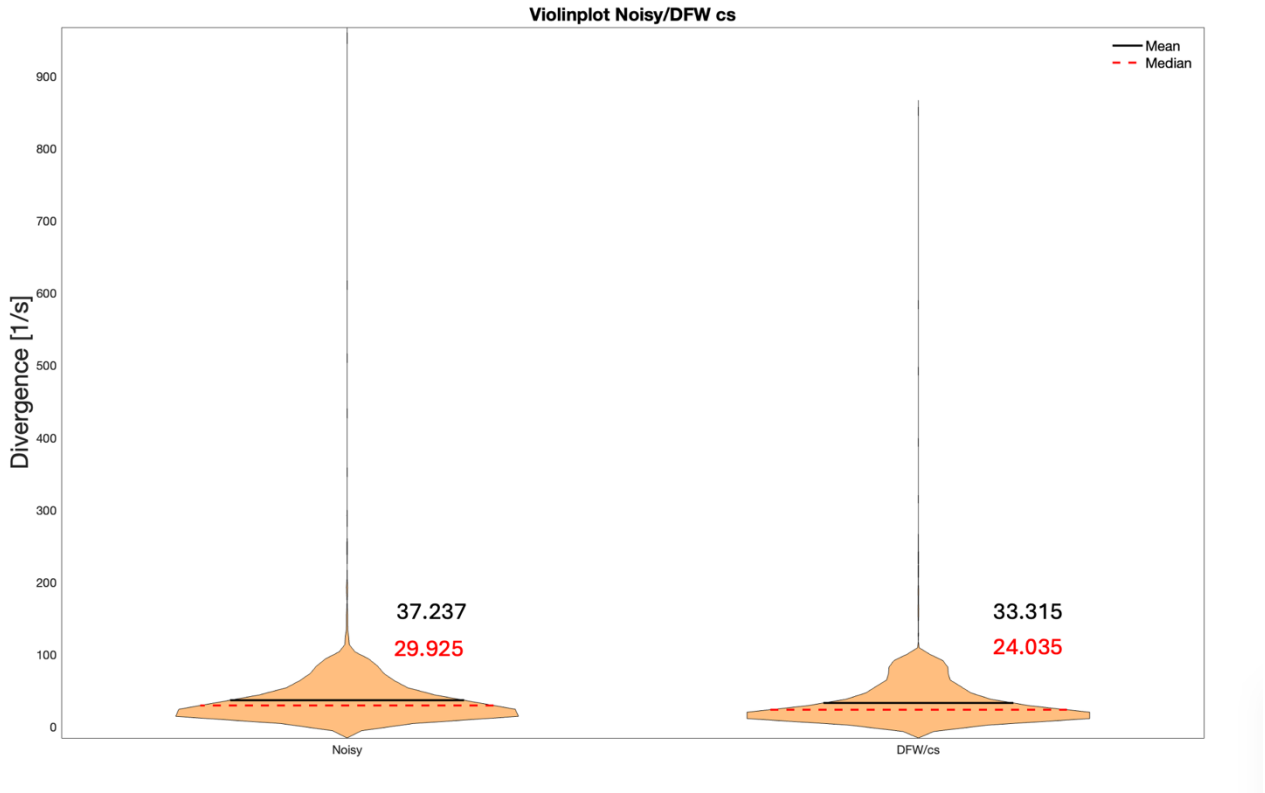

Figure 34. Plot of absolute value of divergence in a violin plot: on the left noisy divergence probability density distribution, on the right divergence probability density distribution of filtered data with DFW-based method and partial cycle spinning.

CONCLUSIONS

This study compares the performances of four state-of-the-art methods for processing 4D flow MRI data with the aim of increasing spatio-temporal resolution, and attenuating acquisition noise. 4D flow MRI is a state-of-the-art imaging technique in the assessment of hemodynamic patterns within the heart and great vessels, which has several limitations that preclude its use as a diagnostic technique in clinical practice. The two main drawbacks are poor spatio-temporal resolution and long acquisition times: to reduce the acquisition time, subsampling techniques arise. However, they give rise to other artifacts and further reduce the spatio-temporal resolution. In this regard, to reduce errors caused by acquisition problems or noise, some approaches exploit the law of conservation of mass for blood, which is an incompressible fluid, to suppress the velocity divergence that should ideally be zero.

Four of the main state-of-the-art divergence-free denoising methods were analyzed, namely: the Finite Difference Method (FDM), the Radial Basis Functions-based method (RBFs), the Divergence-Free Wavelets- based method (DFW) and finally the Divergence-Free Wavelets-based method (DFW) with the implementation of cycle spinning. To compare their performances, these approaches were applied to synthetic 4D flow MRI velocity data obtained from a CFD simulation of a realistic aorta at the systolic peak and after the superimposition of Gaussian white noise.

The Finite Difference Method (FDM) projects the velocity data into a divergence-free space using Helmholtz-Hodge decomposition, solved by employing first-order finite differences with periodic boundary conditions to solve the Laplace equation. Instead, Radial Basis Functions (RBFs)-based method used normalized convolution to locally approximate the acquired velocity field into divergence-free radial basis functions (RBFs), used as convolution kernels. In this circumstance one can choose a larger kernel size, which results in efficient denoising in the vessel lumen. This, together with the possibility of choosing appropriate certainty and applicability functions, makes the RBFs-based method perform better than FDM. Nevertheless, both FDM and RBFs-based method suffer from inaccuracies in the segmentation of the flow field, since the divergence-free constraint on the flow field is strictly imposed: while flow patterns were reconstructed accurately in the vessel lumen, relatively large errors remained at the vessel border.

Divergence-Free Wavelets (DFW)-based method applies the Discrete Wavelet Transform, realized through a bank of filters, separately, to each velocity component. The resulting divergence-free and non–divergence-free coefficients, linearly combined, provide a sparse representation of flow data, which were subjected to the denoising procedure using a soft-thresholding technique, called SureShrink. Instead of eliminating nondivergence-free coefficients, soft-thresholding non-divergence-free coefficients allows the flexibility to adjust the cutoff so that important components, such as those arising near edges, can be captured. Furthermore, a second-generation denoising method, named “cycle spinning”, was considered to reduce blocking artifacts.

The main results showed that both DFW and RBF based methods show significant noise reduction in vector visualization. Visually, their vector representations look very similar to

the original flow field. On the other hand, FDM shows less improvement than other methods. Comparing to DFW without cycle spinning DFW with partial cycle spinning reduces blocking artifacts and improves denoising performance. Comparative analysis of these methods, demonstrated, both qualitatively and quantitatively, the effective restoration of the reference flow field and a reduction in the divergence of noisy data. Quantitative results showed that the DFW-based method performed better than FDM and RBF-based method. The no-divergence constraint in the DFW-based method is more relaxed, making it less sensitive to segmentation errors. Moreover, the DFW-based method with partial cycle spinning further enhanced its performance. DFW with partial cycle spinning outperforms other methods quantitatively, in all the error criteria, and qualitatively.

The good performance of the denoising algorithms investigated in this study open the way for the widespread use of 4D flow MRI in clinical practice, with the advantages that could follow in the treatment of cardiovascular diseases or cardiac surgical procedures. Hemodynamic descriptors, such as those based on wall shear stress (WSS) and its variability in magnitude and direction along the cardiac cycle and other harmonic descriptors such as Fluctuating Kinetic Energy (FKE) could be more accurately calculated using adequately denoised 4D flow MRI data. These hemodynamic parameters make it possible to synthesize information about the highly complex blood flow within vessels, especially near the walls, and its role in the biomechanical processes involved in vascular pathogenesis. In this regard, a possible future development of this work is the search for new denoising techniques, even more performant and less sensitive to segmentation errors, so that a more precise calculation of hemodynamic descriptors such as WSS can be performed from 4D flow MRI data, to assess non-invasively in vivo the flow imprint on the vessel walls and increase the mechanistic knowledge of vascular disease.

BIBLIOGRAFIA

[1] Gasteigder et.al. Visual Exploration of Cardiovascular Hemodynamics (2014).

[2] A. Can, R. Du. Association of hemodynamic factors with intracranial aneurysm formation and rupture: systematic review and meta-analysis. Neurosurgery (2015).

[3] A.M. Nixon, M. Gunel, B.E. Sumpio. The critical role of hemodynamics in the development of cerebral vascular disease: a review. Neurosurgery (2010).

[4] Maya Gabbour, Susanne Schnell, Kelly Jarvis, Joshua D Robinson, Michael Markl, Cynthia K Rigsby. 4-D flow magnetic resonance imaging: blood flow quantification compared to 2-D phase-contrast magnetic resonance imaging and Doppler echocardiography. Department of Medical Imaging, Chicago, IL, 2014.

[5] Rose MJ, Jarvis K, Chowdhary V, Barker AJ, Allen BD, et al. Efficient method for volumetric assessment of peak blood flow velocity using 4D flow MRI. J. Magn. Reson. Imaging, 2016.

[6] Compressed Sensing in DSC-MRI. Università degli studi di Padova (2012).

[7] F. Bistolfi, Campi Magnetici in Medicina, ch. 15. ed. Minerva Medica, 1986.

[8] J. Hornak, The basics of MRI. 1996.

[9] David T.Wymer, Kunal P. Patel, William F. Burke, Vinay K. Bhatia. Phase-Contrast MRI: Physics, Techniques, and Clinical Applications. RadioGraphics 2020.

[10] Joachim Lotz, Christian Meier, Andreas Leppert, Michael Galanski. Cardiovascular Flow Measurement with Phase-Contrast MR Imaging: Basic Facts and Implementation. RadioGraphics 2002.

[11] Michael Markl, Alex Frydrychowicz, Sebastian Kozerke, Mike Hope and Oliver Wieben. 4D Flow MRI. Journal of Magnetic Resonance Imaging (2012).

[12] Zoran Stankovic, Bradley D. Allen, Julio Garcia, Kelly B. Jarvis, Michael Markl. 4D flow imaging with MRI. Cardiovascular Diagnosis and Therapy (2014).

[13] Gilles Soulat, Patrick McCarthy and Michael Markl. 4D Flow with MRI. Annual Review of Biomedical Engineering (2020).

[14] Petter Dyverfeldt, Malenka Bissell, Alex J. Barker, Ann F. Bolger. 4D flow cardiovascular magnetic resonance consensus statement. Journal of Cardiovascular Magnetic Resonance (2015).

[15] Malenka M. Bissell, Francesca Raimondi, Lamia Ait Ali, Bradley D. Allen. 4D Flow cardiovascular magnetic resonance consensus statement: 2023 update. Journal of Cardiovascular Magnetic Resonance (2023).

[16] Walker PG, Cranney GB, Scheidegger MB, et al. Semiautomated method for noise reduction and background phase error correction in MR phase velocity data. J Magn Reson Imaging 1993;3:521-30.

[17] Markl M, Bammer R, Alley MT, et al. Generalized reconstruction of phase contrast MRI: analysis and correction of the effect of gradient field distortions. Magn Reson Med 2003;50:791-801.

[18] Tamas Alexy, Jon Detterich, Philippe Connes, Kalman Toth, Elie Nader, Peter Kenyeres, Jose Arriola-Montenegro, Pinar Ulker and Michael J. Simmond. Physical Properties of Blood and their Relationship to Clinical Conditions. Frontiers in Physiology, july 2022.

[19] R. B. Bird, R. C. Armstrong, and O. Hassager. Dynamics of polymeric liquids. Wiley, 1987.

[20] Sacchi A. Operatori funzionali vettoriali. Sviluppo Progetti Avanzati – R&D Dept.

[21] Jess H. Brewer, *Divergence of a Vector Field*, su *Vector Calculus*, 7 aprile 1999.

[22] Eric W. Weisstein, *Gradiente*, in *MathWorld*, Wolfram Research.

[23] Ali Bakhshinejad. Novel Algorithms for Merging Computational Fluid Dynamics and 4D Flow MRI. *University of Wisconsin-Milwaukee, August 2018.*

[24] S. M. Song, S. Napel, G. H. Glover, and N. J. Pelc. Noise reduction in three-dimensional phase-contrast MR velocity measurements. Journal of Magnetic
Resonance Imaging, 3(4):587-596, jul 1993.

[25] Harsh Bhatia, Gregory Norgard, Valerio Pascucci and Peer-Timo Bremer. The Helmholtz-Hodge Decomposition—A Survey. IEEE Transactions on visualization and computer graphics (2013).

[26] Gunnar Farneback. Polynomial Expansion for Orientation and Motion Estimation. Department of Electrical Engineering, Linkopings universitet, Sweeden (2002).

[27] J. Busch, D. Giese, L. Wissmann, and S. Kozerke. Reconstruction of divergence-free velocity fields from cine 3D phase-contrast flow measurements. Magnetic Resonance in Medicine, 69(1):200-210, jan 2013.

[28] Henrik Haraldsson, Lars Wigstrom, Magnus Lundberg, Ann F. Bolger, Jan Engvall, Tino Ebbers and John-Peder Escobar Kvitting. Improved Estimation and Visualization of Two- Dimensional Myocardial Strain Rate Using MR Velocity Mapping. Journal of Magnetic Resonance Imaging 28:604–611 (2008).

[29] Svenja Lowitzsch, Approximation and Interpolation Employing Divergence-Free Radial Basis Functions with Applications, Ph.D. thesis, Texas A&M University, May 2002.

[30] F. Ong, M. Uecker, U. Tariq, A. Hsiao, M. T. Alley, S. S. Vasanawala, andM. Lustig. Robust 4D flow denoising using divergence-free wavelet transform. Magnetic resonance in medicine, 73(2):828-842, feb 2015.

[31] Ong F, Uecker M, Tariq U, Hsiao A, Alley MT, Vasanawala SS, Lustig M. Improved visualization and quantification of 4D flow MRI data using divergence-freewavelet denoising. In IEEE 10th International Symposium on Biomedical Imaging (ISBI), 2013, USA, 2013. pp. 1186–1189.

[32] A.Bovik, The essential guide to Image Processing, Academic Press, 2009.

[33] I.Daubechies, Ten lectures on Wavelets, CBMS-NSF Regional Conference Series in Applied Mathematics.

[34] Erwan Deriaz, Margarete O. Domingues, Valerie Perrier, Kai Schneider and Marie Farge. Divergence-free wavelets for coherent vortex extraction in 3D homogeneous isotropic turbulence. February, 2007.

[35] Donoho DL, Johnstone IM. Adapting to unknown smoothness via wavelet shrinkage. J Am Stat Assoc 1995;90:1200–1224.

[36] Luisier F, Blu T, Unser M. A new sure approach to image denoising: interscale orthonormal wavelet thresholding. IEEE Trans Image Process 2007.

[37] Fei Xiao, Yungang Zhang. A Comparative Study on Thresholding Methods in Wavelet- based Image Denoising. Procedia Engineering (2012).

[38] A. Temizel and T. Vlachos. Image resolution upscaling in the wavelet domain using directional cycle spinning. Journal of electronic imaging, June 2005.

[39] R.R. Coifman and D.L. Donoho. Translation-Invariant De-Noising. Yale University and Stanford University, 1995.

[40] Xiaochen Wang, Harry J. Carpenter, Mergen H. Ghayesh, Andrei Kotousov, Anthony C. Zander, Marco Amabili, Peter J. Psaltis. A review on the biomechanical behaviour of the aorta. Journal of the Mechanical Behavior of Biomedical Materials, may 2023.

[41] Cira Rosaria Tiziana di Gioia, Andrea Ascione, Raffaella Carletti and Carla Giordano. Thoracic Aorta: Anatomy and Pathology. Diagnostics, june 2023.

[42] D'amati, G.; Leone, O.; Nistri, S.; Roghi, A.; Angelini, A.; Basso, C.; Biagini, E.; Colombo, E.; Mele, D.; Pepe, G.; et al. Paradigm shifts in aortic pathology: Clinical and therapeutic implications. Biology and pathology of the aortic wall. *G. Ital. Cardiol.* **2013**, *14*, 97–109.

[43] P. D. Tafti, R. Delgado-Gonzalo, A. F. Stalder, and M. Unser. Variational enhancement and denoising of flow field images. In 2011 IEEE International Symposium on Biomedical Imaging: From Nano to Macro, pages 1061-1064. IEEE, mar 2011.

[44] E. Bostan, S. Lefkimmiatis, O. Vardoulis, N. Stergiopulos, and M. Unser. Improved Variational Denoising of Flow Fields with Application to Phase-Contrast MRI Data. IEEE Signal Processing Letters, 22(6):762-766, jun 2015.

[45] E. Bostan, O. Vardoulis, D. Piccini, P. D. Tafti, N. Stergiopulos, and M. Unser. Spatio-temporal regularization of flow fields. In 2013 IEEE 10th International Symposium on Biomedical Imaging, pages 836-839. IEEE, apr 2013.

[46] Joaquín Mura, A. Matías Pino, Julio Sotelo, Israel Valverde, Cristian Tejos, Marcelo E. Andia, Pablo Irarrázaval, and Sergio Uribe. Enhancing the Velocity Data From 4D Flow MR Images by Reducing its Divergence. IEEE Transactions on medical imaging, Vol. 35, NO. 10, October 2016.

[47] Qi Gao, Xingli Liu, Hongping Wang, Peng Wu, Mansu Jin, RunJie Wei, Wei Wang, Zhaozhuo Niu, Shihua Zhao, Fei Li. Optimization of 4D flow MRI velocity field in the aorta with divergence-free smoothing. International Federation for Medical and Biological Engineering 2021. Medical & Biological Engineering & Computing, july 2021.